NOVA SCHOOL OF SCIENCE & TECHNOLOGY

DEPARTAMENT OF MATERIAL SCIENCE

BRUNO MARTINS MENDES

MSc in Micro and Nanotechnology Engineering

Cellulose Nanocrystal Based Chiral Structures for Photonic Applications

MASTERS IN MICRO AND NANOTECHNOLOGY ENGINEERING

NOVA University Lisbon

November 2022

NOVA SCHOOL OF SCIENCE & TECHNOLOGY

DEPARTAMENT OF MATERIAL SCIENCE

Cellulose Nanocrystal Based Chiral Structures for Photonic Applications

BRUNO MARTINS MENDES

Master in Micro and Nanotechnology Engineering

Adviser: Doctor Diana Gaspar
Senior Researcher, AlmaScience

Co-advisers: Professor Luís Pereira
Associate Professor, FCT-NOVA Univeristy of Lisbon

Examination Committee:

Chair: Doctor Helena Godinho,
Associate Professor with Habilitation, FCT-NOVA University of Lisbon

Rapporteurs: Doctor Susete Fernandes,
Senior Researcher, FCT-NOVA University of Lisbon

Adviser: Doctor Diana Gaspar,
Senior Researcher, AlmaScience

Professor Luís Pereira,
Associate Professor, FCT-NOVA University of Lisbon

MASTER IN MICRO AND NANOTECHNOLOGY ENGINEERING

NOVA University Lisbon
November 2022

Cellulose Nanocrystal Based Chiral Structures for Photonic Applications

ACKNOWLEDGMENTS

Finally, the deed is done, throughout a hard-fought battle, racing against the clock, but not alone, not in the slightest. This work was completed, not only by me but by all the people who helped, encouraged, and supported me.

I'd like to express my gratitude to FCT-NOVA, Center of Investigation in Materials (CENIMAT), Centro de Excelência em Microeletrónica e Processos Optoelectrónicos (CEMOP-UNINOVA), and to CELLECTIVE project (PTDC/CTM-CTM/4653/2021) for providing the funds, materials, and space for this thesis to be possible.

I would like to thank the FunPaper Lab team (Inês, Madalena, Mariana, Tomás, Cristina and Maria), to whom I owe a lot for always keeping me on my toes and on top of my work (even when I wanted to sleep…) and taking the time help me every time I needed the most.

To my advisors, Doctor Diana, and Doctor Paul, not only you gave me the tools to do what I love, you were great friends, and I can't thank you enough for the support and lessons you gave, and mostly for the patience you had to put up with me.

Family also provided great encouragement and kept me going, even in moments of uncertainty. Mom and Dad, if not for you I would not be here writing this, I hope I can give back everything you gave me throughout these years, I know you got my back and I know I can count on you for everything anytime. This road was not easy, but you fought valiantly and always kept your head high and stood tall. I wish I can be half of what you were to me. To my cousin, João, or should I say brother, you are an OG in my life, and we better keep It that way. From kicking handmade balls against grandad's gate to writing my thesis you were there with me, and life wouldn't be the same without you bro, thank you.

To my college friends (Bruno, Amaral e Rui), thank you for some of the best time spent on this campus. For the night-outs, the evening study sessions, and the long talks when needed (and the fuse ball session!), you were there for me, carrying me through this journey.

Finally, to Hugo, Fred, Raquel e Sofia, an enormous thank you sincerely, I cannot find the words to describe how important you are to me. Through many highs and lows, for the last 10 years you stood beside me and help me build the person I am today. It has been an amazing journey, seeing all of you grow up and thrive and taking me with you through it as

provided me with some of the moments of my life. And to that I think our traditional "petisco" is in order!!

If all days were good days, there would be no good days.

ABSTRACT

This thesis documents the fabrication and characterization of flexible ultraviolet (UV) sensors based on cellulose nanocrystals (CNC) as photonic films, for circularly polarized light sensing. The produced films exhibit an inherent left-handed chiral nematic structure which can be used as a filter for CPL in the visible range, where left CPL is reflected and right CPL is transmitted (LCPL and RCPL, respectively), creating a photonic bandgap. This property will be one of the focuses of the final device, allowing the production of specific electronic outputs depending on the polarization of the irradiating light. One of the main objectives of this work is the modulation of the photonic bandgap using potassium hydroxide, allowing for the tunability of the workable spectrum (near-UV to red visible light). The second objective is the implementation of the photonic film into a UV sensor capable of distinguishing between R- and LCPL. The sensing layer is a zinc oxide (ZnO) ink with carbon contacts, deposited by screen-printing. The device was then encapsulated between cellulose acetate and characterized. Optical characterization shows a blue shift of the photonic bandgap with the addition of potassium hydroxide (from 700 nm with no substitutions to 430 nm with 150% substitution) resulting in a near-linear relation between the photonic bandgap and increasing addition of the hydroxide without relevant modification in the structure of the crystal. Electrical characterization presents an electronic signal distinction between left and right CPL ranging from 5-15%.

Keyword: Cellulose Nanocrystals, Photonic Crystal, Liquid Crystal, Flexible Optoelectronics, Ultraviolet Sensor.

RESUMO

A seguinte tese documenta a fabricação e caracterização de sensores ultravioleta (UV) em substrato flexível com base em celulose nano-cristalina na forma de filmes fotónicos, tornando possível reconhecer diferentes polarizações de luz circularmente polarizada (LCP). Os filmes produzidos exibem uma estrutura quiral nemática esquerda capaz de filtrar LCP na gama da luz visível, onde LCP direita é refletida e LCP esquerda é transmitida (LCPD e LCPE, respetivamente), criando assim um hiato fotónico. Esta propriedade vai ser o foco do funcionamento do dispositivo final, possibilitando a produção de sinais eletrónicos distintos para as diferentes polarizações de luz incidida. Um dos principais objetivos deste trabalho é a modificação do hiato fotónico usando hidróxido de potássio, possibilitando uma modulação do espetro trabalhado (gama entre *near*-UV e visível). O segundo objetivo é a implementação do filme fotónico num sensor UV capaz de distinguir entre LCPD e LCPE. A camada sensível é produzida usando tinta de óxido de zinco (ZnO) e contactos de carbono, depositados através de *screen-printing*. O dispositivo foi encapsulado entre acetato de celulose e caracterizado. Analisando os resultados da caracterização ótica foi possível identificar uma transição do hiato fotónico para o azul com a adição do hidróxido de potássio (de um hiato nos 700 nm sem substituições para 430 nm com a substituição de 150%) resultando numa relação quási-linear entre o hiato fotónico e o aumento de hidróxido de potássio adicionado, sem alterações relevantes na estrutura do cristal. Caracterização elétrica revela uma distinção de sinal elétrico entre as duas polarizações entre 5-15%.

Palavras-Chave: Celulose Nano-cristalina, Cristais Fotónicos, Optoelectrónica Flexível, Sensores Ultravioleta.

CONTENTS

1 MOTIVATION 1

2 STATE OF THE ART 3

3 INTRODUCTION 4

3.1 Introduction to Cellulose 4

3.2 Cellulose Nanocrystals 5

3.2.1 CNC Liquid Crystal 6

3.2.2 CNC Photonic Crystals 6

3.3 CNC Based Ultraviolet Sensor 8

4 METHODS AND MATERIALS 9

4.1 Production Techniques 9

4.2 Device production and assembly 9

4.3 Characterization Techniques 10

5 RESULTS AND DISCUSSION 13

5.1 Optical Analysis 13

5.2 Structural Analysis 15

5.3 Elementary Analysis 17

5.4 Electrical Characterization 21

5.4.1 Non-Encapsulated Sensor Characterization 22

5.4.2 Encapsulated Sensor Characterization 24

5.4.3 Flexible Sensor Characterization 26

6 CONCLUSIONS AND FUTURE PERSPECTIVES 31

6.1 Final Conclusions 31
6.2 Future Perspectives 32
BIBLIOGRAPHY 33
A ANNEXES 37
A.1 Electrical Characterization 37

LIST OF FIGURES

Figure 1 - Cellobiose molecular structure. 4
Figure 2 - Hierarchical structure from a cellulose source represented as cotton (a) to cellulose nanocrystals (e). (adapted from [25],[26]). 5
Figure 3 - Expected interaction between CPL and CNC photonic crystal: a) schematic representation of the expected organization of the CNC and its pitch, and b) spectrophotometry analysis of CNC photonic crystal for L and RCPL. The inset shows Polarized Optical Macroscopy images of L and RCPL. 7
Figure 4 - Schematic of the two device structures ZnO Down (Left) and ZnO Up (Right). 10
Figure 5 - a) Transmittance spectrophotometry spectra (dashed lines represent RCPL and full lines represent LPCL) and b) representation of the linear tendency of the photonic bandgap with the increase in KOH concentration. 14
Figure 6 - X-ray diffractograms of the CNC photonic crystals. 15
Figure 7 - Cross-section of a CNC-150 photonic film. 17
Figure 8 - a) FTIR full spectra of samples from CNC-H to CNC-150 and b) ampliation of relevant regions of the spectra. 18
Figure 9 - Raman spectra of the CNCs samples. 19
Figure 10 - XPS analysis of CNCs photonic films: O 1s (left column), deconvoluted C 1s (center column) and S 2p (right column) spectra of a) CNC-150, b) CNC-125, c) CNC-100, d) CNC-H and e) CNC-Na. 21
Figure 11 - Schematic of non-encapsulated sensor (ZnO down on the left, and ZnO up on the right). 22
Figure 12 - Electrical characterization of both non-encapsulated sensor architectures..... 23
Figure 13 - Schematic of an encapsulated sensor (ZnO Down). 24
Figure 14 - Electrical characterization of both encapsulated sensor architectures. 25
Figure 15 - Electrical characterization for both CPL polarizations for ZnO Down sensor encapsulated architecture..... 27

Figure 16 - a) Schematic of a flexible sensor and b) e c) images demonstrating the flexibility of the device. 28
Figure 17 - Electrical characterization for both CPL polarizations for flexible sensor (tON=60s and tOFF=90s). 28
Figure 18 - a) and c) LCPL and RCPL images of the flexible sensor at 0° from incident radiation, respectively. b) and d) LCPL and RCPL images of the flexible sensor at 20°. e) a cross-section of the flexible sensor and f) magnification of a region of interest. 30
Figure A1 - Electrical characterization of the flexible sensor, for both CPL polarizations and time intervals. 37

LIST OF TABLES

Table 1 - Data from Transmission Spectrophotometry and circularly polarized light macroscopy images. 14
Table 2 - Crystallinity index and crystallite size of the CNCs photonic crystals, from the diffractograms. 16
Table 3 - Elemental analysis of the CNC films. 17
Table 4 - ΔI, t_{rise} and t_{fall}, and R for a non-encapsulated sensor with tON=20s and tOFF=20s. 23
Table 5 - ΔI, t_{rise} and t_{fall}, and R for a non-encapsulated sensor with tON=60s and tOFF=90s 24
Table 6 - ΔI, t_{rise} and t_{fall}, and R for an encapsulated sensor with tON=20s and tOFF=20s. 25
Table 7 - ΔI, t_{rise} and t_{fall}, and R for an encapsulated sensor with tON=60s and tOFF=90s. 26
Table 8 - ΔI, t_{rise} and t_{fall}, and R for the ZnO Down architecture encapsulated sensor with RCPL and LCPL. 27
Table 9 - ΔI, trise and tfall, and R for the flexible sensor with RCPL and LCPL. 29

ACRONYMS

ATR-FTIR	Attenuated Total Reflectance - Fourier Transform Infrared Spectroscopy
CNC	Cellulose Nanocrystals
CPL	Circular Polarized Light
EDS	Energy Dispersive Scanning
EISA	Evaporation Assisted Self-Assembly
FTIR	Fourier Transform Infrared Spectroscopy
FWHM	Full Width at Half Maximum
LC	Liquid-Crystal
LCPL	Left Circularly Polarized Light
PET	Polyethylene terephthalate
POM	Polarized Optical Microscopy
PVA	Polyvinyl Alcohol
RCPL	Right Circularly Polarized Light
SAC	Strong Acid Cation
SEM	Scanning Electron Microscopy
UV	Ultraviolet
XPS	X-Ray Photoelectron Spectroscopy
XRD	X-Ray Diffraction

SYMBOLS

$\bar{n}$	Average Refractive Index
°	Degree
μm	Micrometer
Å	Angstrom
at.%	Atomic Percentage
cm	Centimeter
CNC-H	Cellulose Nanocrystals with Hydrogen Ions as the counter-ion
CNC-Na	Cellulose Nanocrystals with Sodium Ions as the counter-ion
CNC-X	Cellulose Nanocrystals with Potassium Ions as the counter-ion in X percentage
cosθ	Cosine of an angle θ
D	Crystallite Size
eV	Electron-Volt
$\mathbf{I_{(002)}}$	Intensity of the peak representing the crystallographic plane (200)
$\mathbf{I_{am}}$	Intensity of the amorphous region
$\mathbf{I_c}$	Crystallinity Index
K	Shape Factor
KOH	Potassium Hydroxide
kV	Kilovolt
M	Concentration unit of measure - Molar

nm	Nanometer
P	Pitch Length
wt%	Percentage by Weight
ZnO	Zinc Oxide
β	Full Width at Maximum Height of the peak of the crystallographic plane (200)
ΔCPL	Response Difference between Left and Right Circularly Polarized Light
θ_{inc}	Angle between incident light and the normal to a surface
λ	Wavelength
λ_{max}	Maximum Wavelength of the Photonic Bandgap

1

MOTIVATION

Nowadays, technology has become highly customer driven, with the demand for miniaturized devices with the same or better functionality than ever, which in turn, result in an increase in the use of scarce and non-recyclable materials, resulting in e-waste, one of the most predominant challenges of the 21st century.[1]

The field of lightweight, flexible, and cost-effective devices has become a hot topic for research, pioneering novel applications and sustainable alternatives for those materials.

Within this context, aspects as the ecological cost must be considered and there is an opportunity to shift this paradigm with the introduction of natural and nature-inspired nanostructures in new devices capable of serving the needs of different fields.

Observing nature, cellulose becomes a viable solution to these challenges, being the most abundant biopolymer on the planet. Cheap, sustainable, and recyclable, cellulose has gained great relevance in scientific research due to its intrinsic physiochemical properties, creating viable eco-friendly options to fossil-fuel derived and scarce materials.

One cellulosic material capable of serving these needs is cellulose nanocrystals (CNCs), obtained by the acid hydrolysis of biomass. These nanocrystals can self-organize into chiral nematic structures, behaving like a photonic crystal, perfect for its integration in miniaturized photonic and optoelectronics.

The CNC photonic crystals present unique properties regarding their interaction with light such as iridescence and selective transmission to circularly polarized light (CPL). This creates an opportunity for the development of optoelectronic devices capable of distinguishing between CPL polarizations, while being cost-effective and sustainable.

.

2

STATE OF THE ART

Cellulose nanocrystals, or CNCs, have been highly targeted by researchers for their sustainability and wide range of applications throughout various industries [2]. While in suspension, CNC's have been reported to behave as a liquid-crystal and present unique optical properties [3], [4]. The liquid crystal presents a chiral nematic phase based on the rod-like shaped particles, creating a left-handed twisted superstructure [3]. By evaporating the water from the suspension, it is possible to preserve this superstructure in the solid state, producing an iridescent membrane/film [5].

The dried film presents selective transmission to circularly polarized light (CPL), where right-handed light is transmitted and left-handed light is reflected [6]. This phenomenon is true for a wavelength band (photonic bandgap), relative to the pitch of the film, as reported by DeVries et al. [7]. The photonic bandgap has been reported to be modifiable, throughout the infra-red and visible spectrum, by altering the pitch, either through mechanical or chemical methods [8]. Research reports on the influence of suspension concentration on the pitch, due to the lyotropic nature of the liquid-crystal suspension [9]. Further works report on the use of electrolytes for a photonic bandgap shift [10], [11].

These films have been reported to be processed to become multi-stimuli responsive and integrated into devices, capable of transducing the stimuli [12]–[16]. Their integration into optoelectronic and photonic devices has also been reported with devices capable of distinguish between CPL polarizations [10], [17], [18].

Works regarding the applications of CNC films in flexible optoelectronics have been reported, both as a substrate and as a dielectric [19].

3

INTRODUCTION

Being the most abundant biopolymer on the planet, cellulose has been a research topic across various fields, not only due to its physiochemical properties, as will be covered in later chapters, but also for its renewable and sustainable nature. With an eco-friendly approach and sustainability in mind, the integration of cellulose in electronics came as an opportunity to deviate from commonly used materials, such as silicon or scarce metals that are environmental threats due to their difficult reuse and non-viable recycling methods.

3.1 Introduction to Cellulose

Cellulose is a linear syndiotactic homopolymer [20] composed of repeating anhydrous glucose units, connected by β-(1-4)-glycosidic bonds [21], also known as cellobiose ($[C_{12}H_{20}O_{10}]_n$) (Figure 1). A cellulose chain presents a 3D ribbon-like structure due to its glucosidic bonds, the extra hydrogen bonds between the oxygen atoms present in the rings and the three OH groups (intramolecular bonds)[9]. Through hydrogen and Van der Waals bonds to other cellulose chains (intermolecular bonds), the chain stability is improved.

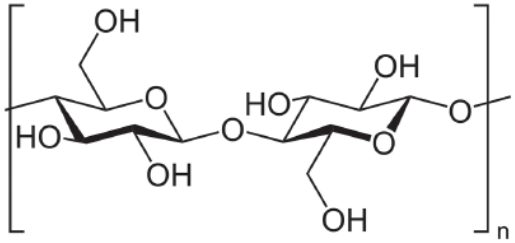

Figure 1 - Cellobiose molecular structure.

Cellulose is a non-toxic, bio-degradable bio-polymer and present properties such a high mechanical strength, alterable optical and electrical characteristics [22].

Naturally produced by plant cells to form their walls (Figure 2a and 2b) (but also from bacteria and fungi [23]), cellulose can be extracted in the form of fibers. These fibers are composed of microfibrils (Figure 2c) intertwined with other biopolymers (such as lignin and hemicellulose). Due to their polymerization process, they present even smaller fibrils, known as nanofibrils, with repeating patterns of amorphous and crystalline regions.

Through mechanical, chemical routes or by combining both, these fibrils can be downsized into microfibrils (Figure 2c) or into crystal-like structures, known as microcrystalline cellulose (Figure 2d). Although maintaining some amorphous content, this derivate of cellulose presents an high crystalline content resulting in a chemically stable structure with the properties already mentioned [24].

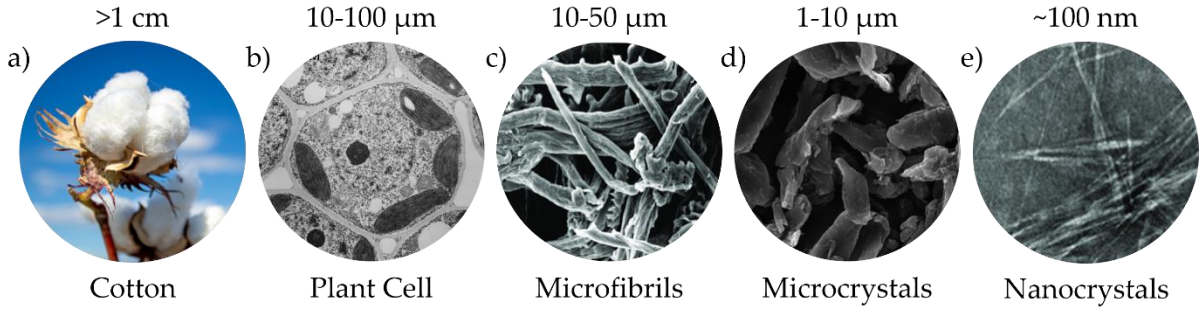

Figure 2 - Hierarchical structure from a cellulose source represented as cotton (a) to cellulose nanocrystals (e). (adapted from [25],[26]).

3.2 Cellulose Nanocrystals

Cellulose Nanocrystals (CNCs) (Figure 2e) can be obtained by isolating the crystalline domains present in cellulose microfibrils or microcrystalline cellulose. For this work, the CNCs used were purchased to CelluForce whose process is based on acid hydrolysis of softwood pulp in sulfuric acid. This approach follows Gray et al. work, which favors the hydrolysis of disordered regions (amorphous), leaving highly ordered cellulose in rod-shaped nanoparticles[27], [28]. Many factors in this process can alter CNCs physiochemical properties such as particle dimensions, surface charge, density and functional groups [29], [30]. After hydrolysis, the CNC suspension is dialyzed, separated from acid residues and neutralized to sodium hydroxide (NaOH) [27], leaving CNCs with a surface containing sulfate groups with sodium counter-ions [9].

CNCs have high aspect ratios and long surface area, controlled by the hydrolysis process. In addition to those characteristics, they also present unique properties such as the ability to align in magnetic [31], and electrical fields [32] and self-assembly into chiral nematic liquid crystalline phases [33].

3.2.1 CNC Liquid Crystal

As stated before, CNCs tend to form chiral nematic liquid crystal (LC) phases, when in a suspension. CNC liquid crystals are described as lyotropic where the suspension can produce both isotropic and anisotropic phases, depending on their concentration [10]. According to works previously developed [9], it was found that the concentrations which gave the highest yield of the anisotropic phase were between 4.5-5.5 wt%, presenting an almost 50/50 volume fraction between both phases. This process was assisted by sonication, to break down agglomerates and increase system entropy, resulting in a distinct interface between phases.

A chiral nematic phase is a specific nematic phase that occurs when anisotropic particles adopt high orientational ordering but no positional ordering between their neighbors due to the inherent particle chirality, inducing chirality to the nematic phase. It is assumed that CNCs presents an inherent right-handed chirality (at a molecular level) ([17], [34]), when in suspension tend to self-assemble into a left-handed chiral nematic superstructure. The resulting anisotropic LC presents various interactions with electromagnetic waves such as iridescence, selective reflection of circularly polarized light and circular dichroism [17].

3.2.2 CNC Photonic Crystals

As previously mentioned, CNC anisotropic suspensions are optically active leading to a great candidate for optoelectronic uses, though, as a fluid it is difficult to find applications in the field. Fortunately, these properties can be retained in solid form as a phonic crystal.

When left to dry, the anisotropic phase starts to lose orientational order while positional order starts to rise, forming tactoids [35]. This process is known as Evaporation Induced Self-Assembly (EISA) and its final product is a mesoporous photonic crystal based in CNCs. During EISA, as the water contents starts to lower the suspension viscosity starts to increase and thus reducing particle movement (lower kinetic energy), locking the chiral nematic structure in place. Conventionally, the chiral nematic phase can be represented as individual layers twisting along an axis, following a director, where a 360° rotation of the director represents the pitch. Although the structure is preserved, so are all the defects and misalignments resulting from the tactoid formation, hindering the final photonic properties [9]. Using drop-cast, one of the challenges found in EISA, which influences the optical properties of the crystal, is the formation of a so-called "coffee-ring" where CNCs migrate to the edge boundaries, resulting in unpredictable optical properties due to the disordered structure [36], [37]. This occurs when a drop of suspension is left to dry with no physical boundaries, except the air on top of it.

For this work, one of the main characteristics presented by these crystalline structures is their interaction with circularly polarized light (CPL), as selective light transmission/reflection, and structural color. Circularly polarized light is a specific type of light polarization, obtained by superimposing two linear polarized light waves with equal frequencies [38], resulting in a wave following a vector (along the x-axis) with a perpendicular vector rotating at a constant rate (in the zy plane). The rotation orientation of the latter determines the handedness of the light wave, either left or right CPL (LCPL and RCPL, respectively).

The dried film presents a photonic bandgap highly dependent on the pitch. A theoretic photonic bandgap, λ_{max}, can be determined following the DeVries equation:

$$\lambda_{max} = \bar{n}P\cos\theta_{inc} \text{ (Equation 1)}$$

where $\bar{n}$ is the average refractive index, P is the pitch length and θ_{inc} is the angle between the incident light and the normal of the film (the director vector of the chiral nematic structure).

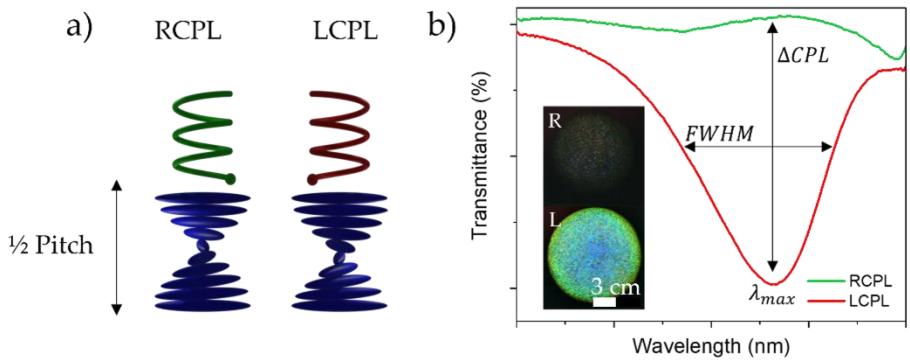

Figure 3 - Expected interaction between CPL and CNC photonic crystal: a) schematic representation of the expected organization of the CNC and its pitch, and b) spectrophotometry analysis of CNC photonic crystal for L and RCPL. The inset shows Polarized Optical Macroscopy images of L and RCPL.

Controlling the pitch allows for the blue or red shift of the photonic bandgap (demonstrated in Figure 3b), within a certain range of wavelengths (normally in the visible spectrum). Various methods have been shown to alter the pitch in the various stages of the film, from pre-deposition treatments to drying environments [36]. Studies show successful pitch modification through additives, such as ionic salts [39] and organic molecules [40]. Later in this thesis, ionic salts will be the focus for pitch and photonic bandgap modification with the use of potassium hydroxide (KOH). The structural color is also highly dependent on the pitch and its interaction with incident light. Due to pitch lengths in the same order of magnitude of visible light, CNC photonic crystals present vivid iridescent structural colors [41]. This property can

also help in assessing the photonic bandgap visually, without the use of spectrophotometry, through Polarized Optical Microscopy (POM) and Polarized Optical Macroscopy.

3.3 CNC Based Ultraviolet Sensor

From the properties assessed in previous sections, a question arises regarding the application of these crystals. Along with many other fields of research, optoelectronics can take the most out of the optical characteristics of CNC-based photonic films. For this work, a device was designed with them in mind. Appling the photonic crystals' selective transmission/reflectance for a traditional ultraviolet (UV) sensor, it is possible to formulate a device capable of sensing CPL. The wavelength range of these devices, near UV range typically operating around 400 nm, require a suitable sensing material, such as zinc oxide (ZnO).

Zinc Oxide is a *n*-type semiconductor, non-expensive, non-toxic and chemically stable [42] with a bandgap between 3.2-3.4 eV and high exciton binding energies at room temperature [43]. Due to its UV photoresponse, ZnO has been used as a sensing layer in many UV sensing devices. However, this material presents some intrinsic drawbacks such as slow response and recovery speed [42]. As a solution to those downsides, researchers have been studying ways to increase surface area to amplify the sensing capabilities of ZnO. Nanostructures of ZnO were one of the ways researchers found to achieve the ideal properties [44], [45]. This lead to an increase in photoresponse, sensitivity and reduction of active area (allowing for device miniaturization) , depending on the morphology of ZnO particles [46]. In the ZnO the UV sensing process occurs when the oxygen molecules, present on the semiconductor metal oxide surface, capture free electrons present in the *n*-type semiconductor and form a depletion layer [42]. When exposed to UV, the high energy photons (energies above the bandgap of zinc) photogerenerate electron-hole pairs which migrate to the surface, creating an electrical signal. This process is highly dependent on the environment of the sensing layer as demonstrated by Tian et al [47]. The absence of any gas in the working environment may hinder UV sensing. The electrical signal can be retrieved by any conductive material but for this work carbon-based ink was applied to maximize the interface between the two.

For this work were tested two structures of sensors. In the following chapters, the devices produced will be presented in detail and the electrical characterization will be discussed.

Many UV ZnO-based sensors have been successfully tested and some ever commercialized, which show great promise as a sensing layer for the devices studied in this thesis [48], [49].

4

METHODS AND MATERIALS

This chapter describes the fabrication steps from the initial CNC suspension to the final encapsulated device and the characterization techniques applied to each context.

4.1 Production Techniques

For this thesis, the CNCs used were purchased to CelluForce with 180 nm in length and 4-5 nm thick (data provided by the supplier). The crystals were dispersed in deionized (DI) water to form a 5 wt% suspension. The suspension was sonicated using the VCX 500 Ultrasonic Processor at 60% power, using a tapered tip, for one hour for each 15g of suspension and then filtered through a 1.6 μm glass fiber filter. The filtered suspension was left to rest until full phase separation occurred and the anisotropic phase was removed (CNC-Na) using a Pasteur's pipet. Using a Strong Acid Cation (SAC), the Na^+ ions were exchanged with a proton (H^+) to form CNC-H. After this ionic trade, the suspension was filtered again. To accurately measure the suspension's concentration, thermogravimetric analysis was conducted. A 1.5 M KOH solution, in DI water, was prepared, and a specific volume was added to 1 g of suspension to obtain each required concentration for the ionic trade, replacing the proton with a potassium counter-ion (K^+), creating the suspensions CNC-X, where X is the replacement percentage (CNC-25 to CNC-150).

To produce the photonic crystals, the method chosen was drop-casting due to its ease of application. Before casting, the substrate surface was exposed to UV radiation for 15 minutes using a Novascan PSD-UV with ozone elimination system, with a mechanical mask, leaving a hydrophilic area, to increase wettability providing the best area of substrate/suspension volume ratio. The drops were then left to dry in a low temperature and high humidity environment (3-5 °C) to lower the evaporation rate and enhance the self-assembly process.

4.2 Device production and assembly

A 5 wt% PVA (MW = 20-30k g/mol) solution was produced in DI water at 60 °C.

A 5 wt% cellulose acetate (MW = 30k g/mol) solution was produced in acetone at room temperature.

In a glass substrate, a layer of PVA solution followed by a layer of cellulose acetate solution was applied using the K101 Control Coater System with a 120 µm knife. The drop-cast methodology mentioned before was applied to form the photonic crystals, using a 1 cm x 1 cm mechanical mask.

ZnO ink was prepared using commercial ZnO particles and an isotropic 5 wt% CNC dispersion at a 40-60% ratio, respectively. Using a manual screen-printing setup, two structures were built (as presented in Figure 4):

- A 0.5 cm x 0.5 cm square of UV-sensitive ZnO ink was printed on top of the crystal, followed by printing carbon-based ink for electrical contacts (denominated ZnO Down).

- The carbon-based ink electrical contacts were printed first and then the 0.5 cm x 0.5 cm square of UV-sensitive ZnO ink (denominated ZnO Up).

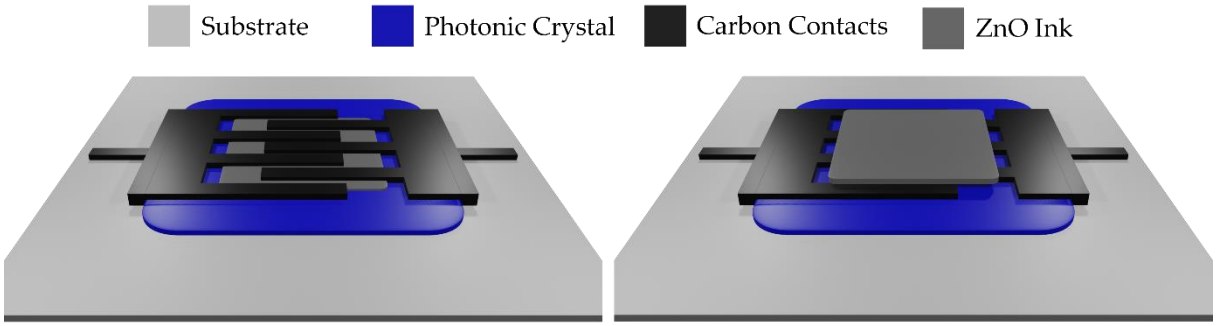

Figure 4 - Schematic of the two device structures ZnO Down (Left) and ZnO Up (Right).

To be able to reach the contacts, the contacts were elongated to ease electrical characterization. Both structures were encapsulated by a cellulose acetate layer using the same method as the first layer.

4.3 Characterization Techniques

The variation in coloration under CPL illumination of the photonic crystals was analysed using Polarized Optical Microscopy (POM) using the Optical Stereo Microscope Leica M80, both using polarizers for CPL. Transmission Spectrophotometry using Spectrometer UV-Vis-NIR Shimadzu UV 3101pc with a custom circular light polarizer setup from 400-800nm was used to measure the photonic band gap, spectral width and ΔCPL. The spectral range was established at 400 nm due to the absorbance effect of the polymeric filters, hindering the readings for more energetic wavelengths.

Crystallographic analysis was performed by X-ray Diffraction (XRD) using PANalytical X/Pert Pro in Bragg-Brentano geometry with Cu-Kα radiation (λ=1.5406 Å) to retrieve data regarding crystallinity peaks, sample crystallinity and crystallite size. Pitch length and cross-section imaging were obtained using the Hitachi Regulus 8220 FE-SEM.

Energy Dispersive Scanning (EDS) associated to a Scanning Electron Microscope (SEM) using Tabletop Microscope TM3030 Plus Hitachi, with a 5000x magnification and a 15kV tension, was used to chemically analyse the samples, acquiring data regarding their elemental composition. X-ray Photoelectron Spectroscopy (XPS) was conducted to also analyse samples' surface chemical composition with the intent of quantifying and identifying specific bonds and groups using the Kratos AXIS Supra with a monochromatic Aluminium source. To further improve the chemical analysis, Fourier Transformed Infra-Red Spectroscopy (FTIR) and Raman Spectroscopy analysis were conducted. FTIR was operated in attenuated total reflection (ATR) using Spectrum Two ranging from 600-4000 cm^{-1}, allowing the comparison of functional groups between data gathered and bibliography, for cellulose-based materials. Raman Spectroscopy using Reninshaw Qontor, with a 532 nm laser, was used as a complementary study of FTIR spectroscopy, not only to corroborate previous analysis but also to study specific bands (S-O groups at 850 cm^{-1}).

Electrical characterization was performed using an Agilent 4155C semiconductor parameter analyser with the Everbeing C-2 Mini manual probe station. The radiation source in use was a ThorLabs 365 nm laser diode, with 3.1 mW intensity with a current bias of 500 mA.

5

RESULTS AND DISCUSSION

As described in section 1.2.2, the pitch can be modified using ionic salts. The addition of KOH to the anisotropic liquid crystalline phase can tune the pitch to a near-UV range where the device can function as a filter for a UV sensor. This chapter presents the results of the characterization of the films produced with the aforementioned suspensions and their application in an optoelectronic device.

5.1 Optical Analysis

To study the influence of KOH on the pitch and photonic bandgap of the CNC films, a sweep of concentrations was used, and the produced films were analyzed by transmission spectrophotometry and circularly polarized imaging. For this study, several films were prepared using the 5 wt% anisotropic suspension and the 1.5M solution of KOH. As presented in Table 1, spectrophotometry analysis demonstrated a blue shift of the bandgap with the increase in KOH concentration, reaching a bandgap near the UV region for CNC-150. ΔCPL were lower than expected but remained constant across all samples, with values between 30-40%. ΔCPL is responsible for the electrical signal distinction between LCPL and RCPL in the final device, the higher it is the better this distinction.

As for Full Width at Half Maximum (FWHM) or spectral width, the cells with "*" represent values that were not possible to determine, as the spectra are incomplete in the range of defined wavelength. This property defines how sharp is the photonic bandgap, which influences how the final device responds to incident light.

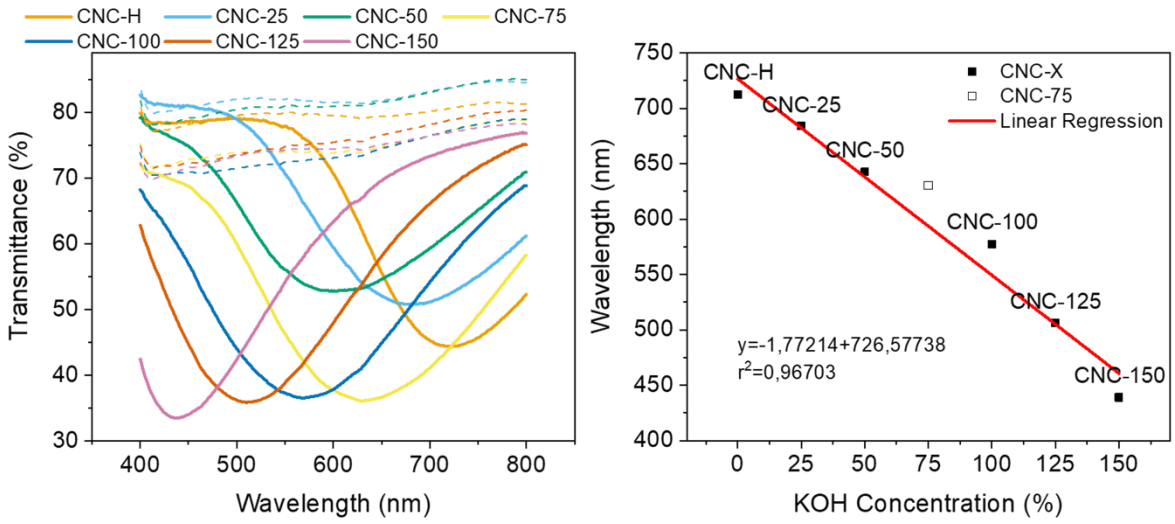

Figure 5 - a) Transmittance spectrophotometry spectra (dashed lines represent RCPL and full lines represent LPCL) and b) representation of the linear tendency of the photonic bandgap with the increase in KOH concentration.

Table 1 - Data from Transmission Spectrophotometry and circularly polarized light macroscopy images.

	CNC-Na	CNC-H	CNC-25	CNC-50	CNC-75	CNC-100	CNC-125	CNC-150
λ_{max} (nm)	666	723	678	648	630	568	510	437
FWHM (nm)	*	*	*	267	264	243	215	*
ΔCPL (%)	34.5	36.3	31.8	35.9	37.8	35.98	38.0	37.3
LCPL	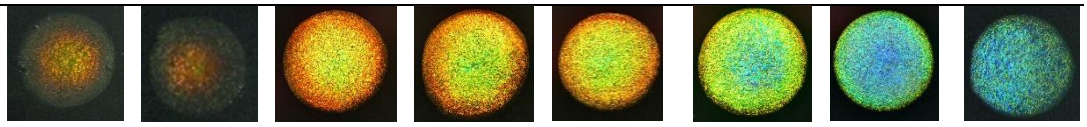							
RCPL	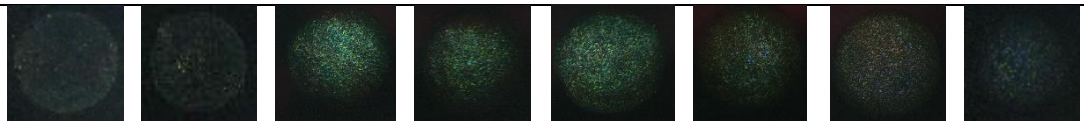							

Circularly polarized imaging analysis was performed with a 20° slope and demonstrates an increase of blue crystalline regions with higher KOH concentrations, reaching a full blue crystal in CNC-150. CNC-Na and CNC-H do not reflect such vivid colors as the other crystals because their photonic bandgap is in the near infrared regions of the visible spectrum and thus resulting in a semi-transparent film, when irradiated with LCPL. Due to the optimization of the EISA process in a low temperature and high humidity environment (for low evaporation

rate), the coffee-ring effect is not evident, resulting in uniform coloration throughout the samples.

In Figure 5a, a blue shift of the photonic bandgap is evidenced with spectrophotometry analysis, in line with Table 1. The spectra present a constant ΔCPL and, although not calculated for all samples, a decrease in spectra width with the addition of KOH. Also, as can be observed, the sample CNC-75 has a photonic bandgap almost parallel to CNC-50, not following the linear tendency presented in Figure 5b. This led to the exclusion of the sample from the study, this sample will not be appearing in further characterization. The remaining samples fit the linear regression.

5.2 Structural Analysis

Knowing how the photonic bandgap varies with KOH concentration, other questions arise regarding the crystalline structure of the crystal and how the addition of potassium dopants influences its crystallinity. Using XRD, it is possible to infer the crystallinity index and crystallite size.

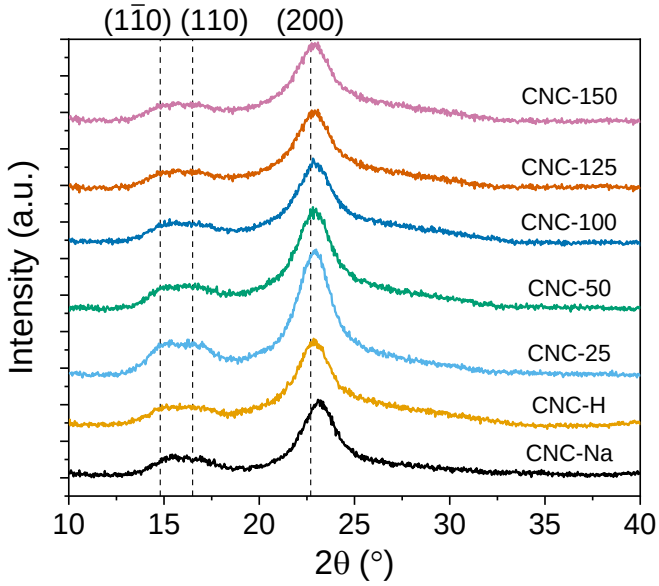

Figure 6 - X-ray diffractograms of the CNC photonic crystals.

The X-Ray diffractograms, represented in Figure 6, demonstrate the typical main peaks representing the three characteristic crystallographic planes of cellulose, (1$\bar{1}$0), (110) and (200), at 14.5°, 16.5° and 22.5°, respectively [50].

With the data gathered, the degree of crystallinity (I_c) and the crystallite size (D) were calculated following Segal et al work [51] and the Scherrer equations (Equation 2.1 and 2.2,

respectively). The I_c represents the fraction that is occupied by the ordered CNCs when compared to the amorphous regions. This study will help understand if the addition of KOH to the suspension has any influence on the crystallographic arrangement of the photonic film, and its influence on the self-assembly.

$$I_c = \frac{I_{(200)} - I_{(am)}}{I_{(200)}} \text{ (Equation 2.1)} \quad D = \frac{K\lambda}{\beta \cos\theta} \text{ (Equation 2.2)}$$

where $I_{(200)}$ is the maximum intensity regarding the (200) peak and $I_{(am)}$ is the minimum in the amorphous region (between 16° and 20°), K is a shape factor (considered as 0.5), λ is the wavelength of the radiation used for the analysis, β is the FWHM of the (200) peak and θ is Bragg diffraction angle.

Table 2 - Crystallinity index and crystallite size of the CNCs photonic crystals, from the diffractograms.

	CNC Na	CNC H	CNC 25	CNC 50	CNC 100	CNC 125	CNC 150
I_c (%)	88.57	87.99	86.36	84.35	84.56	84.76	84.48
D (nm)	6.98	7.02	7.10	6.81	7.00	6.66	6.09

Through the analysis of Table 2, a slight decrease in crystallinity can be observed with the addition of KOH when compared to CNC-Na, but they are still in the same order of magnitude. The crystallite size values fall between the sizes described in Hamad et al work (consistently between 5.8 and 8.3 nm) [52]. This analysis demonstrated minimal influence of the addition of KOH, on the crystallinity of the film while achieving optimal optical properties, as mentioned before.

To assess the structure of the photonic crystals and the CNCs arrangement, a cross-section analysis of a CNC-150 film was performed using Scanning Electron Microscopy (SEM), presented in Figure 7.

In Figure 7, the thickness of the film can be measured, resulting in a 16.5 μm thick film. The chiral nematic structure can be observed and presented as a wave-like texture. Pitch's length could not be assessed due to how the sample was prepared (fractured break in liquid nitrogen).

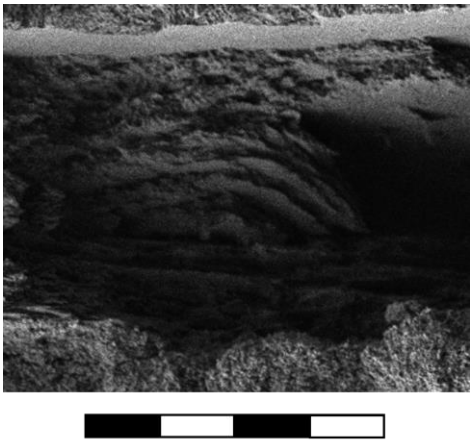

Figure 7 - Cross-section of a CNC-150 photonic film.

5.3 Elementary Analysis

While the addition of dopants, in the form of KOH, does not influence the structural properties of the films, it is expected to observe changes at a chemical level. As mentioned in the Introduction, due to the hydrolysis process with sulfuric acid, CNCs present sulfate groups on their surface. When the first ionic exchange takes place (from CNC-Na to CNC-H) the counter-ion present in those groups changes from Na^+ to H^+. With the addition of KOH, it is expected that the second ionic exchange enables the counter ion change from H^+ to K^+ (from CNC-H to CNC-X).

To ensure the presence of potassium in the samples and quantify it in relation to the sulfur content, an EDS analysis was performed. The results are presented in Table 3.

Table 3 - Elemental analysis of the CNC films.

Elements (at.%)	CNC Na	CNC H	CNC 25	CNC 50	CNC 100	CNC 125	CNC 150
Carbon	54.25	55.18	56.11	56.38	54.85	56.11	53.67
Oxygen	44.93	44.44	43.51	43.11	44.57	43.21	45.56
Sulfur	0.32	0.37	0.29	0.34	0.30	0.33	0.31
Sodium	0.50	-	-	-	-	-	-
Potassium	-	-	0.09	0.17	0.28	0.35	0.45

As summarized in Table 3, the sulfur content is constant across all samples, confirming the existence of sulfate groups on the CNCs surface. The first ionic exchange resulted in a complete change of counter ion, evidenced by the absence of sodium in CNC-H samples. As

the concentration of KOH increases a linear increase in the atomic percentage of potassium is observed, validating the incorporation of K in the CNC films.

To understand how the potassium interacts with the CNCs, two analyses were performed, FTIR and Raman Spectroscopy. FTIR was used for a broader analysis while Raman was used to study specific regions of the spectrum, where FTIR resolution was lacking.

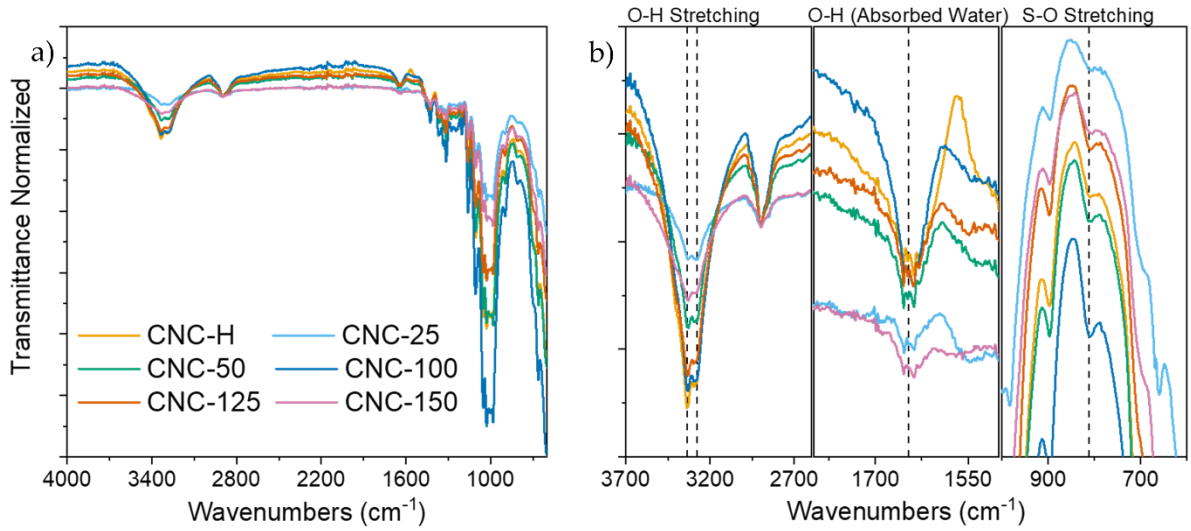

Figure 8 - a) FTIR full spectra of samples from CNC-H to CNC-150 and b) ampliation of relevant regions of the spectra.

As presented in the literature [21], [53], CNCs typically present two distinct absorbance regions. The first region appears at higher wavenumbers, from 2600 to 3600 cm^{-1} while the second can be found at lower wavenumbers, from 600 to 1800 cm^{-1}, presented in Figure 5a.

The first two bands, at 3330 and 3285 cm^{-1} correspond to the stretching of intra and inter-molecular hydrogen bonds to oxygen, respectively, as seen in Figure 5b. The modifications done by the addition of KOH resulted in a shift and band broadening.

At 2900 cm^{-1}, the stretching of C-H groups is represented. The spectra were normalized to this point because it does not shift significantly with cellulose modifications. The peak at 1640 cm^{-1} is ascribed to H-O-H bending vibrations of water absorbed. From the analysis of this peak, it is possible to retrieve information regarding the successful ionic exchange from H^+ to K^+, where H^+ is replaced by K^+ and bonds to OH^- groups in the suspension, resulting from the KOH dissociation, forming H_2O. Since the spectra are normalized, a direct comparison can be made to assess the relation between KOH addition and the presence of absorbed water. From CNC-25 to CNC-100 a tendency is presented, with the increase of KOH concentration the peak is greater. CNC-125 and CNC-150 present less intense peaks than CNC-100. This is the result of a saturation being reached in CNC-100, where most of the H^+ counter ions were replaced, and further addition of KOH does not affect the sulfate groups directly. Although water is added through higher volumes of KOH solution, this water is evaporated during the EISA

process and thus not altering the peaks for absorbed water. Other characteristic cellulose bands can be observed.

The band absorbed 1426 cm^{-1} is associated with asymmetric C-H_2 vibrations. 1334 and 1314 cm^{-1} C-H_2 and C-OH in-plane bending are presented respectively. The peaks at 1160 and 1105 cm^{-1} are associated with anti-symmetric bridge C-O-C and anti-symmetric in-plane ring stretching, respectively. The bands at 1054 and 1029 cm^{-1} are related to C-C and C-OH stretching vibrations, respectively. These latter bands differ from the literature as they can shift due to cellulose modifications to its structure [21]. Peaks related to sulfate esterification during acid hydrolysis can be found at 1205 and 812 cm^{-1}.

For infrared spectroscopy, low-frequency regions are difficult to interpret due to the existence of several bands. Nevertheless, Raman spectroscopy can be used to infer the response of several functional groups. Raman spectroscopy also uses a radiation which does not interact with water, resulting in a reduction of background noise typically observed in the FTIR [54]. Additionally, this technique was also used to validate the presence of the sulfate groups and their interaction with KOH. For a direct comparison of the spectra, a normalization to all spectra was applied to the highest peak.

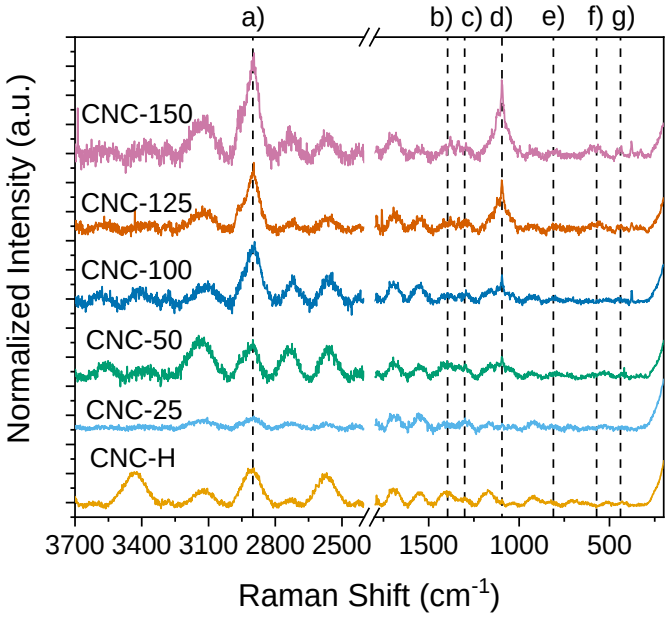

Figure 9 - Raman spectra of the CNCs samples.

According to the literature, CNCs present bands regarding the vibration of sulfate groups and C-O-S bonds [55]. Between 2800 and 2900 cm^{-1}, a band associated with C-H and C-H_2 bonds stretching can be found, represented as a) in Figure 9. In b) it is observed a peak at 1400 cm^{-1}, associated with crystalline cellulose structures.

At lower Raman shifts, the sulfate-related peaks start to appear. Peaks at 1300 and 1080 cm^{-1} are associated with asymmetric and symmetric stretching of O=S=O bonds, repetitively (c and d, accordingly), thus confirming the presence of sulfate groups. As evidenced in the spectra, an increase in sharpness of d), as the KOH concentration increases, can be observed. This is the result of the interaction between the K^+ counter ions and the sulfate groups, altering their vibration. This result can confirm the bonding between the two. The e) peak is the result of C-O-S stretching vibration. Peaks f) and g) are associated with the deformation of O=S=O and SO_3 groups, accordingly. Although it is a small variation in peak height, these peaks also demonstrate the interaction between the K^+ and sulfate groups, as the KOH concentration increases the peaks get sharper.

XPS analysis was used to further characterize the films surface elemental composition and chemical bonding states. This analysis was only performed for CNC-H, CNC-Na, and CNC-100 to CNC-150. The primary objective of this study was to understand how the excess KOH interacted with the CNCs. As expected, the surface analysis indicates high concentrations of carbon and oxygen, since the films are cellulose-based. This analysis resulted in two spectra, low-resolution and high-resolution. The low-resolution spectra present the two main peaks found in cellulose, oxygen, and carbon, at 534 and 286 eV, respectively.

From the analysis of the O 1s band, a major shift can be observed in CNC-H spectra and minor shifts in CNC-100, CNC-125 and CNC-150 spectra (Figure 10, left column) . In CNC-100's spectra, a second component can be observed at lower binding energies, in line with the CNC-H peak. This component was assumed as contributions from remaining sulfate groups not affected by the first ionic exchange.

The deconvolution of C 1s high-resolution spectra, in Figure 10 (center column), present four types of carbon bonds, which can be assigned to C-C/C=C bonds (285.0 eV), C-O-H bonds (286.8 eV), O-C-O bonds (288.5 eV) and O-C=O bonds (289.9 eV). Throughout all samples, both O-C-O and O-C=O peaks remained constant except for CNC-H where O-C=O shifted to higher binding energies. From CNC-100 to CNC-125 and CNC-150, a reduction in the peak intensity of C-C bonds can be observed.

Potassium peaks (K 2p1/2 and 2p3/2) are typically observed near C 1s spectra (at 293.3 or 292.5 eV [56]). However, in this case the potassium peaks are negligible when compared to the C 1s band, thus it is not possible to address properly their analysis. None of the samples (CNC-100 to CNC-150) presented substantial peaks in the assessed bands and thus it was assumed that CNC samples with lower KOH concentrations did not present them as well.

Alternatively, a peak regarding sulfur related bonds were analyzed, as presented in Figure 10 (right column), as S 2p bands, centered at 168.5 eV [10]. The peaks analyzed presented a minor shift to higher binding energies throughout all samples.

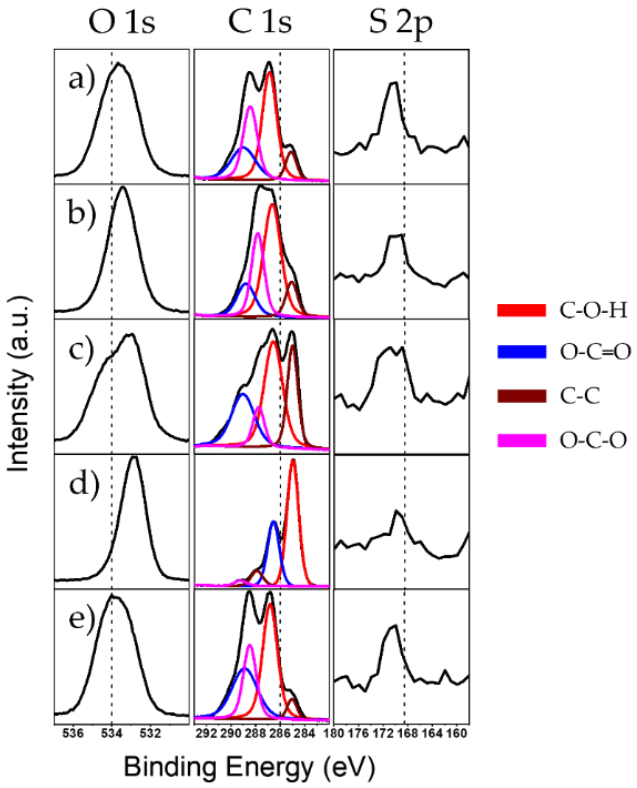

Figure 10 - XPS analysis of CNCs photonic films: O 1s (left column), deconvoluted C 1s (center column) and S 2p (right column) spectra of a) CNC-150, b) CNC-125, c) CNC-100, d) CNC-H and e) CNC-Na.

5.4 Electrical Characterization

From the photonic films assessed in previous characterizations, the CNC-150 presented the best optical characteristics out of all samples, presenting a photonic bandgap closest to the intended sensing spectrum region (around 400 nm). The high potassium concentration did not demonstrate any chemical or structural drawbacks and thus, the final device - a UV sensor - was produced with these films as the filter for incident CPL.

The UV sensors were produced with two architectures, where the position of the ZnO sensing layer changes relative to the photonic crystal and the carbon contacts.

To compare both architectures, three main characteristics were calculated based on the data gathered. The response current (ΔI) is the difference between the current during the OFF stage (dark current, I_{dark}) and the current during the ON stage (maximum photocurrent, I_{ph}), and it is calculated according to Equation 3.1.

Responsivity (R) is the sensor's ability to respond to an incident light, considering the power by area output of the incident radiation (P_{UV}), as demonstrated in Equation 3.2. The switching response is used to evaluate how fast the sensor responds to state switching, ON to OFF (t_{fall}) and OFF to ON (t_{rise}).

$$\Delta I = I_{ph} - I_{dark} \text{ (Equation 3.1)} \quad R = \frac{I_{ph} - I_{dark}}{P_{UV}} \text{ (Equation 3.2)}$$

t_{rise} is the time required to shift from 10 to 90% of I_{ph}, and t_{fall} is the time required to shift from 90 to 10% of I_{ph}. For this analysis, I_{ph} is the average of the peaks on each characterization.

For this characterization, all tests were performed at three voltages (0.5, 1 and 2 V) and using two different ON/OFF cycle times (20/20 s and 60/90 s) to understand the behavior of the device's response time and responsivity with different voltage bias. The analysis had two distinct moments where in the first, the two different architectures (ZnO Up and ZnO Down) were characterized with unpolarized light to assess the best device. In a second moment, the best device was characterized under both CPL polarizations.

The sensors were also characterized in three different moments of production: non-encapsulated, encapsulated with cellulose acetate, and free-standing (after peeling). This study served to analyze the influence of encapsulation on the UV sensor response and to assess the influence of flexible substrates on the structure of the photonic film.

From previous characterizations, CNC-150 was chosen to serve as the photonic layer because it presented greater optical properties without any drawbacks in crystallinity and chemical composition.

5.4.1 Non-Encapsulated Sensor Characterization

For this characterization, the sensors (ZnO Up and ZnO Down) were analysed without any encapsulation, as presented in Figure 11.

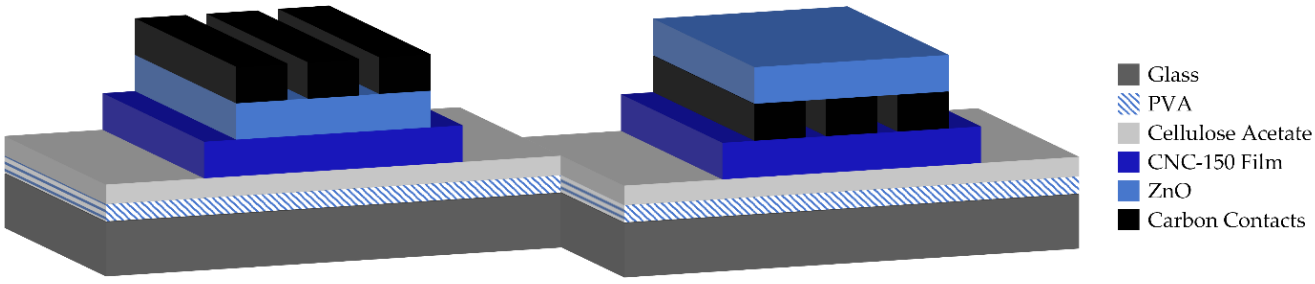

Figure 11 - Schematic of non-encapsulated sensor (ZnO down on the left, and ZnO up on the right).

The samples were characterized with incident light from the underside (incident light irradiates the photonic film first since the goal was to use the CNCs layer as a filter). This

mounting strategy helped uniformize the results since, in the final device, the light will irradiate firstly through the film as well.

To serve as a baseline for future analysis, both non-encapsulated architectures were characterized under a 365 nm laser diode. The P_{UV} for this analysis was 31.44 mW/cm², measured with an optometer.

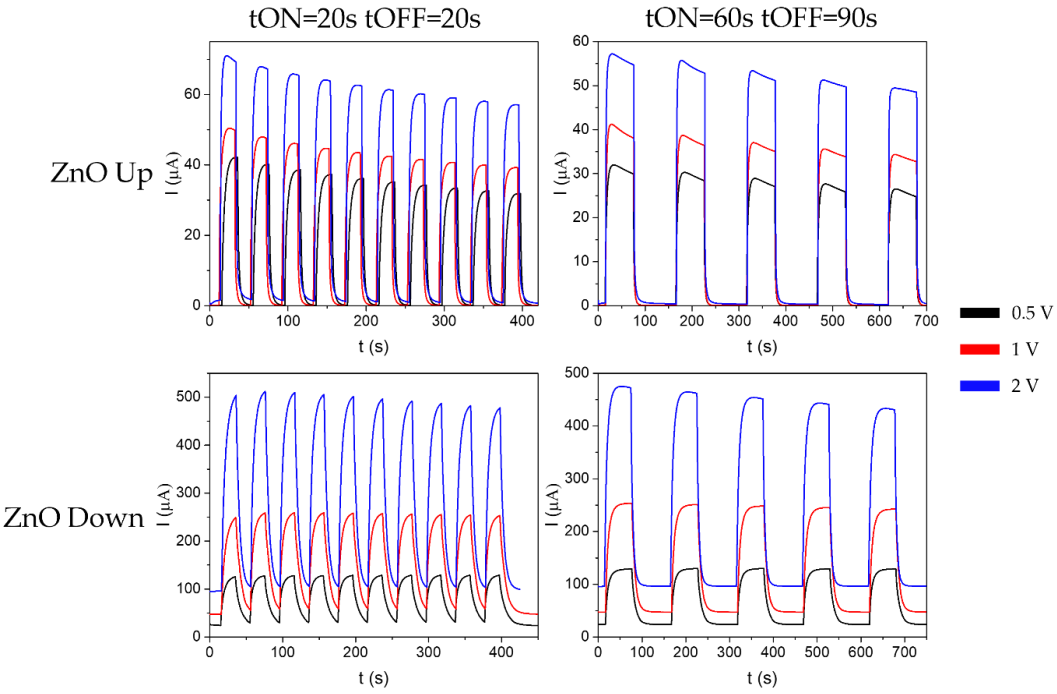

Figure 12 - Electrical characterization of both non-encapsulated sensor architectures.

Using the equations mentioned above (Equations 3.1 and 3.2), the data was extracted from the graphs' analysis, (presented in Figure 12) and ΔI, t_{rise} and t_{fall} were calculated and presented in Tables 4 and 5.

Table 4 - ΔI, t_{rise} and t_{fall}, and R for a non-encapsulated sensor with tON=20s and tOFF=20s.

Architecture	ZnO Up			ZnO Down		
Bias Voltage (V)	0.5	1	2	0.5	1	2
ΔI (µA)	36.1	43.6	61.9	97.9	198	393
t_{rise} (s)	6.5	5.25	3.4	7.3	8.5	9
t_{fall} (s)	4	2.5	2.5	13.5	12.5	9.4
R (µA/mW)	1.15	1.39	1.97	3.11	6.28	12.50

Table 5 - ΔI, t_{rise} and t_{fall}, and R for a non-encapsulated sensor with tON=60s and tOFF=90s

Architecture	ZnO Up			ZnO Down		
Bias Voltage (V)	0.5	1	2	0.5	1	2
ΔI (μA)	29.1	37.4	53.1	106	199	359
t_{rise} (s)	6.25	4.5	1.9	13.75	14.9	12.1
t_{fall} (s)	3	2	2.5	18.3	15.2	9.1
R (μA/mW)	0.92	1.19	1.69	3.37	6.34	11.40

As expected, although presenting higher response times, ZnO Down has a better current response than ZnO Up. This may be related to a higher irradiated surface of the ZnO sensing layer than the other architecture. With this configuration, the light is transmitted through the photonic film and reaches directly the ZnO, instead of being obstructed by the carbon contacts. Because it presented greater current responses, ZnO Down also presents greater responsivity when compared to ZnO Up.

5.4.2 Encapsulated Sensor Characterization

The device previously characterized was encapsulated in cellulose acetate (as presented in Figure 13) and characterized, following the same analysis parameters as before (P_{UV}=31.44 mW/cm²).

To study the effects of encapsulation on ZnO sensing properties, the electrical characterization followed the same parameters as previously mentioned. Also, since the carbon-based ink, used for the contacts, reacts with stronger solvents, this analysis can assess the effects of the cellulose acetate on the device.

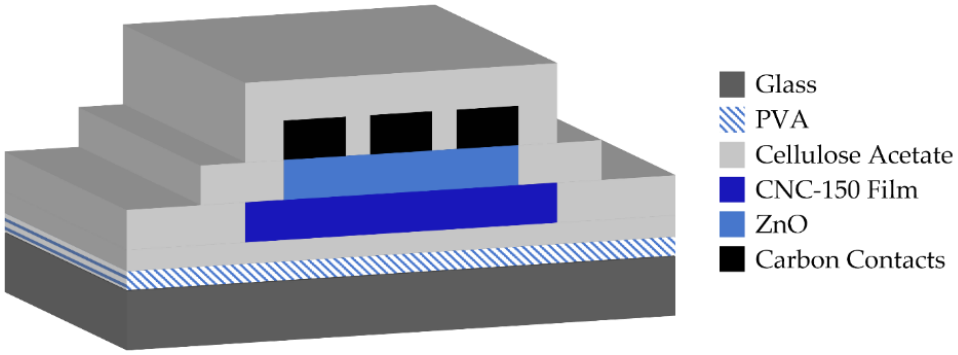

Figure 13 - Schematic of an encapsulated sensor (ZnO Down).

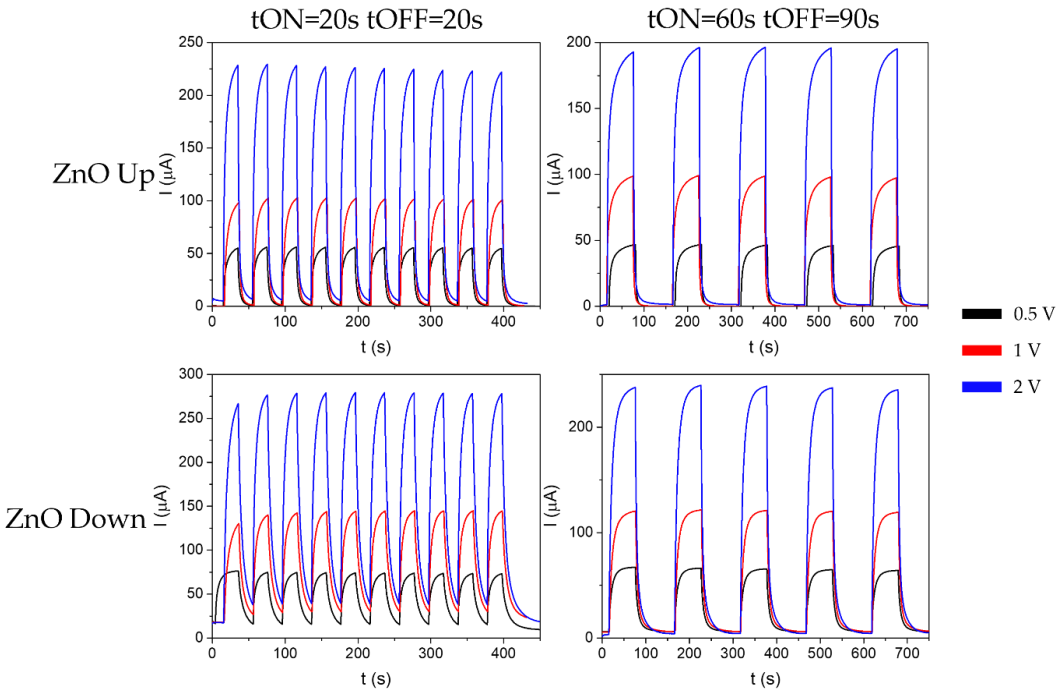

Figure 14 - Electrical characterization of both encapsulated sensor architectures.

Using the equations aforementioned (Equations 3.1 and 3.2), the data was extracted from the graphs' analysis, (presented in Figure 14) and ΔI, t_{rise} and t_{fall} were calculated and presented in Tables 6 and 7.

Table 6 - ΔI, t_{rise} and t_{fall}, and R for an encapsulated sensor with tON=20s and tOFF=20s.

Architecture	ZnO Up			ZnO Down		
Bias Voltage (V)	0.5	1	2	0.5	1	2
ΔI (μA)	54.8	101	221	58.6	115	240
t_{rise} (s)	9.25	8.9	8.3	8.3	8.4	8.9
t_{fall} (s)	5.9	4.5	4.3	12.3	12.5	11.4
R (μA/mW)	1.74	3.22	7.03	1.87	3.65	7.65

Table 7 - ΔI, t_{rise} and t_{fall}, and R for an encapsulated sensor with tON=60s and tOFF=90s.

Architecture	ZnO Up			ZnO Down		
Bias Voltage (V)	0.5	1	2	0.5	1	2
ΔI (μA)	46.4	98.4	195	59.6	115	236
t_{rise} (s)	20.75	21.1	17.6	17.1	16.7	17.8
t_{fall} (s)	4.9	4.9	4.9	16.2	15.4	15.7
R (μA/mW)	1.47	3.13	6.20	1.89	3.66	7.51

Analysing Tables 6 and 7, both characterizations presented a decrease in current response and an increase in response time. As explained in the Introduction, ZnO uses oxygen in the surrounding atmosphere and incident UV radiation to photogenerate electrons, which generate the electric signal. If the device is sealed with a barrier to the oxygen, ZnO cannot function as expected, leading to a decrease in the current response and an increase in response time. Comparing both architectures, ZnO Down still presented greater current responses and responsivity, in line with the data analysed in sub-section 3.4.1.

5.4.3 Flexible Sensor Characterization

Considering the previous characterizations, the architecture which presented better performance was ZnO Down. This led to the adoption of this architecture for the final device.

For a proper comparison between the encapsulated (before peeled off from the glass carrier) and after the peel, an electrical characterization with CPL was performed to the encapsulated device on the glass carrier, resulting in Figure 15, and Tables 8 and 9. Note that the glass carrier was used only for the fabrication of the devices, the final goal of this work was the production of a cellulose-based sensor using a CNCs film as a light filter.

The use of polarizers results in the absorption of some of the radiation before reaching the sample; the P_{UV} was measured once more, reading 0.253 mW/cm² and 0.324mW/cm² for LCPL and RCPL, respectively.

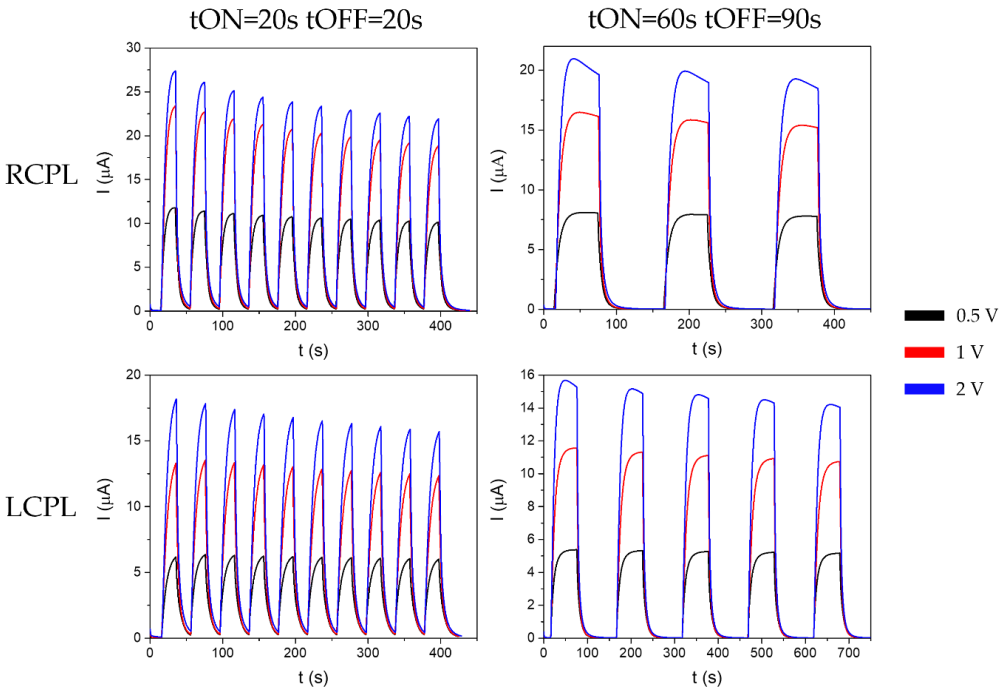

Figure 15 - Electrical characterization for both CPL polarizations for ZnO Down sensor encapsulated architecture.

Using Equations 3.1 and 3.2, ΔI, t_{rise} and t_{fall} were calculated, from the analysis of Figure 15, for both CPL polarizations, RCPL and LCPL, resulting in Table 8.

Table 8 - ΔI, t_{rise} and t_{fall}, and R for the ZnO Down architecture encapsulated sensor with RCPL and LCPL.

Cycles	tON=20s tOFF=20s						tON=60s tOFF=90s					
Parameters	RCPL			LCPL			RCPL			LCPL		
Bias Voltage (V)	0.5	1	2	0.5	1	2	0.5	1	2	0.5	1	2
ΔI (µA)	10.5	20.4	23.4	5.94	12.6	16.3	7.82	15.5	19.4	5.27	11.1	14.9
t_{rise} (s)	9.1	10.2	10	11.1	12.1	11.8	14.5	15	12.9	17.3	19.9	15.1
t_{fall} (s)	8.6	6.6	6.7	11.7	8.7	8.1	11.6	8.2	8.5	14.7	10.2	9.3
R (µA/mW)	41.6	80.7	92.4	18.3	39.0	50.4	30.9	61.2	76.7	16.3	34.3	45.8

As expected, when comparing the two characterizations (non-polarized and polarized) of the device, the polarized analysis presented a decrease in both current response and responsivity due to the decrease in light intensity reaching the sensing layer.

When comparing the signals from RCPL's and LCPL's analysis, the device presented a response decrease from RCPL to LCPL, as expected. This is due to the high reflectivity of the photonic film to LCPL, diminishing the light intensity reaching the sensing layer. A 55-75% difference in current response and 45-60% difference in responsivity (highly dependent on the voltage bias) can be observed when comparing the data from Tables 8 and 9.

To peel off the device from the glass substrate, the sample was bathed in warm water (60 °C) with low agitation to facilitate the dissolution of the PVA layer, thus releasing the flexible sensor from the glass carrier (Figure 16).

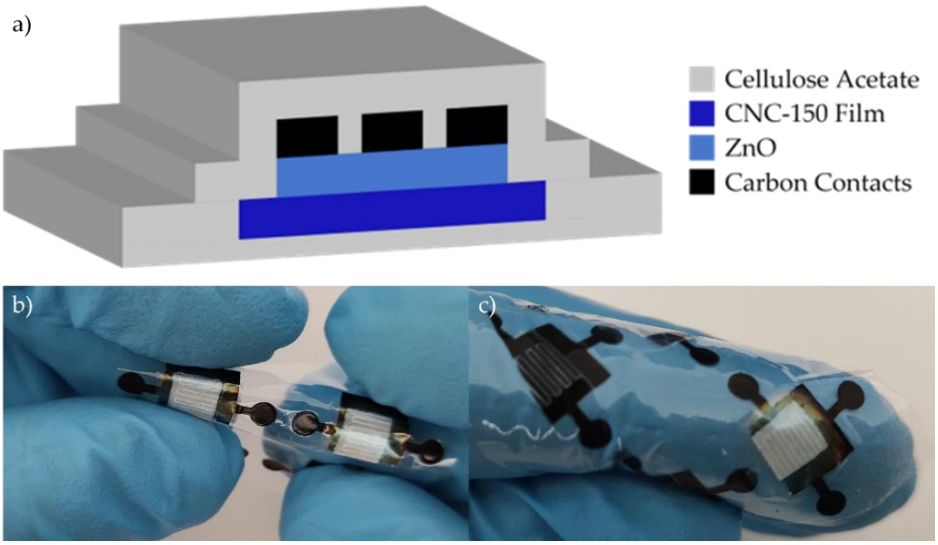

Figure 16 - a) Schematic of a flexible sensor and b) e c) images demonstrating the flexibility of the device.

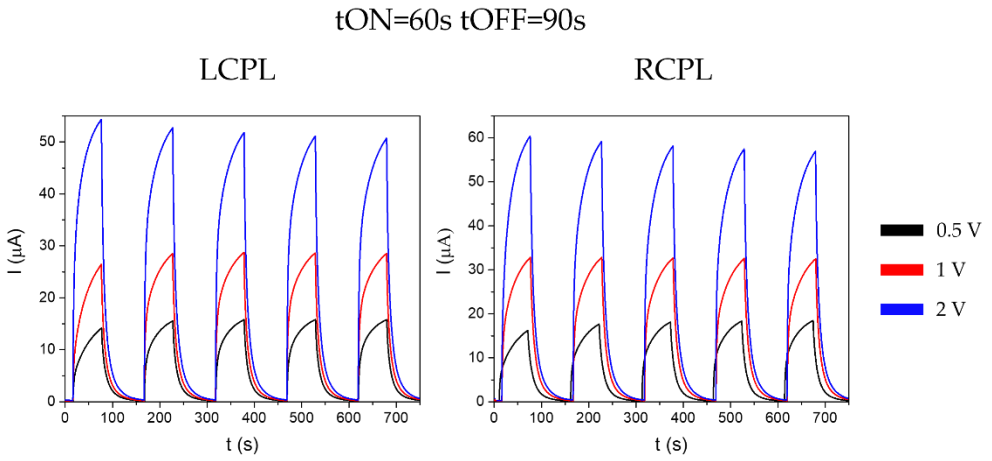

Figure 17 - Electrical characterization for both CPL polarizations for flexible sensor (tON=60s and tOFF=90s).

Using Equations 3.1 and 3.2, ΔI, t_{rise} and t_{fall} were calculated based on the analysis of the graphs presented in Figure 17, resulting in Table 9. The calculations were performed for both CPL polarizations, and both time intervals, although Figure 17 only presents the optimal time interval, tON=60s and tOFF=90s.

Table 9 - ΔI, trise and tfall, and R for the flexible sensor with RCPL and LCPL.

Cycles	tON=20s tOFF=20s						tON=60s tOFF=90s					
Parameters	RCPL			LCPL			RCPL			RCPL		
Bias Voltage (V)	0.5	1	2	0.5	1	2	0.5	1	2	0.5	1	2
ΔI (μA)	13.5	25.1	48.2	13.2	24.5	44.6	18.0	32.5	58.2	15.7	28.6	51.9
t_{rise} (s)	11.1	9.9	10.25	9.4	8.75	8.9	37.2	35	34.7	33.1	33	33.3
t_{fall} (s)	14.5	13.9	13	13.5	13.3	13	26.5	26.1	24.5	27.6	26.4	23.2
R (μA/mW)	4.17	7.75	14.90	5.22	9.70	17.60	5.55	10.00	18.00	6.20	11.30	20.50

Considering the characterization of the encapsulated device on the rigid carrier, the flexible sensor presented a decrease in both current response and responsivity. This may be due to contractions in the flexible substrate, wrinkling the crystal, and hindering its properties (as seen in Figure 18a and b).

As observed in Figures 16b and 16c, the final device maintains its functionality after flexing and the photonic films kept its integrity. Analysing the data calculated from the characterization of the flexible sensor, a 3-12% current response, and 15-20% responsivity differences, were achieved between LCPL and RCPL. As seen in Figures 18a and 18b, the photonic films become opaque to incident LCPL, leading to a decrease in signal response. In Figures 18c and 18d, the films irradiated with RCPL become semi-transparent, uncovering the ZnO sensing layer, leading to a greater signal response.

After its characterization, the flexible sensor was fractured in half for cross-section SEM imaging, resulting in Figures 18e and 18f. The discrete layers, previously mentioned in Figure 16, can be observed.

In Figure 18f, a separation between the ZnO sensing layer and the photonic film can be observed. This separation may be due to contractions during the curing process of the ZnO layer, reducing in size due to solvent evaporation.

Overall, the device presents the expected architecture, without major delamination between layers or intra-layer defects.

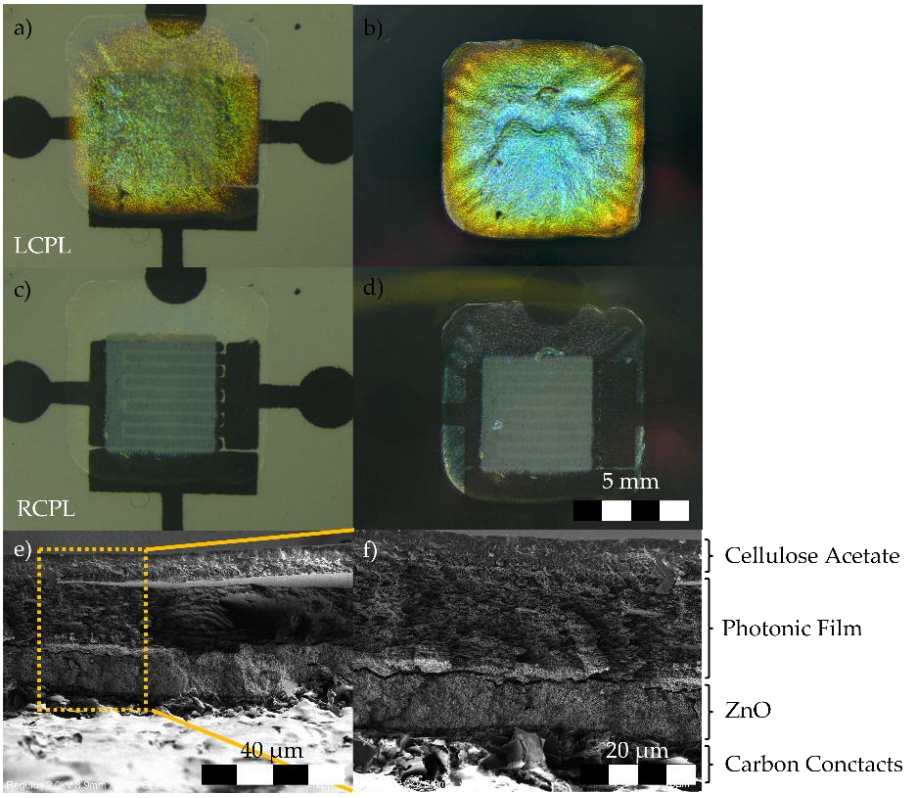

Figure 18 - a) and c) LCPL and RCPL images of the flexible sensor at 0° from incident radiation, respectively. b) and d) LCPL and RCPL images of the flexible sensor at 20°. e) a cross-section of the flexible sensor and f) magnification of a region of interest.

6

CONCLUSIONS AND FUTURE PERSPECTIVES

6.1 Final Conclusions

This thesis focused on the manipulation and characterization of the photonic bandgap of CNC-based photonic films, and their application in fully encapsulated, flexible UV-sensors, capable of CPL sensing.

The used fabrication techniques, such as shear-coating, drop cast and screen printing proved to be of relative simplicity and perfectly suited for these devices' fabrication. Due to the simplicity of the equipment involved, without the need for vacuum systems and other high-cost thin-film deposition techniques (such as sputtering and electron-beam), these processes are low-cost and highly scalable, leading to cheap and mass-produced devices.

A linear tendency was observed relating the photonic bandgap and the alkali solution added, resulting in a blue shift with the increase in KOH concentration. Furthermore, when characterized under CPL, the films presented vivid structural colors related to the photonic bandgap, and it was possible to adjust the photonic bandgap of 437 nm for the CNC-150, becoming the chosen concentration for the filter layer of the sensor.

The tune of the photonic bandgap was made without compromising the crystallinity index (88-84%) or crystallite size (6-7 nm), the latter being in line with the literature.

Chemical analysis confirmed the success of the two ionic exchanges, from Na^+ to H^+ and H^+ to K^+, presenting higher K^+ concentrations for greater additions of KOH. As a side note, the CNC-100 analysis confirmed the calculations performed to exchange all H^+ to K^+, presenting near-equal concentrations of sulfur and potassium.

Raman spectroscopy confirmed bonds of the potassium, being observed the increase of the peak intensity (sulfate groups at bands 1300 and 1080 cm^{-1}) with the addition of KOH

The ultimate goal was the production of devices directly onto the CNCs films. Two architectures were tested (ZnO Up and ZnO Down) at three different assembly stages (non-encapsulated, encapsulated, and flexible). From the analysis of the two different architectures, ZnO Down performed the best, with greater current responses and responsivities. This architecture was applied to the flexible device, presenting a 3-12% current response and 15-20%

responsivity differences, between LCPL and RCPL. Although the results are lower than expected, the performance is related to the radiation used being at a lower wavelength than the photonic bandgap of the crystal, where ΔCPL is not at its peak, resulting in less signal distinction.

6.2 Future Perspectives

As demonstrated throughout this thesis, the study of CNCs as a photonic crystal is still a novelty and presents few implemented applications. Furthermore, the modulation of its photonic bandgap and the means to modify it still require further studies. The use of other types of ions may be an interesting study to assess their effect on the photonic bandgap. A question arises regarding the influence of ion valence and size on the modulation of photonic bandgap. If valence influences the band, would there be a difference between monovalent and polyvalent doping? Does the ion size influence the pitch, and if it does, how does influence it? All these studies of the photonic bandgap can further the specifications of the device studied in this thesis and further devices based on the photonic properties of these films.

Optimizations of the EISA process can also influence the films' optical properties. Controlling the environment where the drying occurs can alter the pitch of the films. As mentioned in the Introduction, CNCs react to external magnetic and electrical fields, which could be of interest to modify the orientation of the CNCs when drying, altering the optical properties.

Taking advantage of the electrochemical properties of CNC films, an electrolyte-gated transistor could also be produced, capable of discrete states for CPL.

Since cellulose-based devices present high sensitivity to humidity (pitch varies with humidity and thus a variation of the bandgap can be observed), with the use of resistance to heat the photonic film in a controlled environment, an electrical modulation of the photonic bandgap could be possible.

BIBLIOGRAPHY

[1] V. Murthy and S. Ramakrishna, "A Review on Global E-Waste Management: Urban Mining towards a Sustainable Future and Circular Economy," *Sustainability*, vol. 14, no. 2, 2022, doi: 10.3390/su14020647.

[2] R. J. Moon, G. T. Schueneman, and J. Simonsen, "Overview of Cellulose Nanomaterials, Their Capabilities and Applications," *JOM*, vol. 68, no. 9, pp. 2383–2394, 2016, doi: 10.1007/s11837-016-2018-7.

[3] R. H. MARCHESSAULT, F. F. MOREHEAD, and N. M. WALTER, "Liquid Crystal Systems from Fibrillar Polysaccharides," *Nature*, vol. 184, no. 4686, pp. 632–633, 1959, doi: 10.1038/184632a0.

[4] R. H. Marchessault, F. F. Morehead, and M. J. Koch, "Some hydrodynamic properties of neutral suspensions of cellulose crystallites as related to size and shape," *J. Colloid Sci.*, vol. 16, no. 4, pp. 327–344, 1961, doi: https://doi.org/10.1016/0095-8522(61)90033-2.

[5] J.-F. Revol, D. L. Godbout, and D. G. Gray, "Solidified liquid crystals of cellulose with optically variable properties." Google Patents, May 13, 1997.

[6] S. N. Fernandes, L. F. Lopes, and M. H. Godinho, "Recent advances in the manipulation of circularly polarised light with cellulose nanocrystal films," *Curr. Opin. Solid State Mater. Sci.*, vol. 23, no. 2, pp. 63–73, 2019, doi: https://doi.org/10.1016/j.cossms.2018.11.004.

[7] H. De Vries, "Rotatory power and other optical properties of certain liquid crystals," *Acta Crystallogr.*, vol. 4, no. 3, pp. 219–226, May 1951, doi: https://doi.org/10.1107/S0365110X51000751.

[8] R. M. Parker *et al.*, "The Self-Assembly of Cellulose Nanocrystals: Hierarchical Design of Visual Appearance," *Adv. Mater.*, vol. 30, no. 19, p. 1704477, May 2018, doi: https://doi.org/10.1002/adma.201704477.

[9] P. Grey, "Cellulose Nanocrystal Chiral Structures for Electronics and Photonics," NOVA School of Science and Technology, Universidade NOVA de Lisboa, 2021.

[10] P. Grey *et al.*, "Ionically Modified Cellulose Nanocrystal Self-Assembled Films with a Mesoporous Twisted Superstructure: Polarizability and Application in Ion-Gated Transistors," *ACS Appl. Electron. Mater.*, vol. 2, no. 2, pp. 426–436, Feb. 2020, doi: 10.1021/acsaelm.9b00652.

[11] X. M. Dong, T. Kimura, J.-F. Revol, and D. G. Gray, "Effects of Ionic Strength on the Isotropic−Chiral Nematic Phase Transition of Suspensions of Cellulose Crystallites," *Langmuir*, vol. 12, no. 8, pp. 2076–2082, Jan. 1996, doi: 10.1021/la950133b.

[12] L. Bai, Z. Wang, Y. He, F. Song, X. Wang, and Y. Wang, "Flexible Photonic Cellulose Nanocrystal Films as a Platform with Multisensing Functions," *ACS Sustain. Chem. Eng.*, vol. 8, no. 50, pp. 18484–18491, Dec. 2020, doi: 10.1021/acssuschemeng.0c06174.

[13] C. Verma, M. Chhajed, S. Singh, and P. K. Maji, "Cellulose Nanocrystals for Environment-Friendly Self-Assembled Stimuli Doped Multisensing Photonics," *ACS Appl. Polym. Mater.*, vol. 4, no. 6, pp. 4047–4068, Jun. 2022, doi: 10.1021/acsapm.2c00061.

[14] Q. Zhu *et al.*, "Stimuli-responsive cellulose nanomaterials for smart applications.," *Carbohydr. Polym.*, vol. 235, p. 115933, May 2020, doi: 10.1016/j.carbpol.2020.115933.

[15] O. Kose, A. Tran, L. Lewis, W. Y. Hamad, and M. J. MacLachlan, "Unwinding a spiral

of cellulose nanocrystals for stimuli-responsive stretchable optics," *Nat. Commun.*, vol. 10, no. 1, p. 510, 2019, doi: 10.1038/s41467-019-08351-6.

[16] S. N. Fernandes *et al.*, "Mind the Microgap in Iridescent Cellulose Nanocrystal Films," *Adv. Mater.*, vol. 29, no. 2, p. 1603560, Jan. 2017, doi: https://doi.org/10.1002/adma.201603560.

[17] P. Grey *et al.*, "Combining Soft with Hard Condensed Matter for Circular Polarized Light Sensing and Logic Operations," *Adv. Opt. Mater.*, vol. 9, no. 6, p. 2001731, Mar. 2021, doi: https://doi.org/10.1002/adom.202001731.

[18] P. Grey *et al.*, "Field-Effect Transistors on Photonic Cellulose Nanocrystal Solid Electrolyte for Circular Polarized Light Sensing," *Adv. Funct. Mater.*, vol. 29, no. 21, p. 1805279, May 2019, doi: https://doi.org/10.1002/adfm.201805279.

[19] D. Gaspar *et al.*, "Nanocrystalline cellulose applied simultaneously as the gate dielectric and the substrate in flexible field effect transistors.," *Nanotechnology*, vol. 25, no. 9, p. 94008, Mar. 2014, doi: 10.1088/0957-4484/25/9/094008.

[20] P. Jain, A. De, and N. B. Singh, "Cellulose-Based Materials for Water Purification," *ChemistrySelect*, vol. 7, no. 24, p. e202200121, Jun. 2022, doi: https://doi.org/10.1002/slct.202200121.

[21] R. S. Dassanayake *et al.*, "Characterization of cellulose nanocrystals by current spectroscopic techniques," *Appl. Spectrosc. Rev.*, vol. 0, no. 0, pp. 1–26, 2021, doi: 10.1080/05704928.2021.1951283.

[22] B. Tosh, "Synthesis and Sustainable Applications of Cellulose Esters and Ethers: A Review," 2014.

[23] L. Brinchi, F. Cotana, E. Fortunati, and J. M. Kenny, "Production of nanocrystalline cellulose from lignocellulosic biomass: Technology and applications," *Carbohydr. Polym.*, vol. 94, no. 1, pp. 154–169, 2013, doi: https://doi.org/10.1016/j.carbpol.2013.01.033.

[24] O. A. Battista and P. A. Smith, "MICROCRYSTALLINE CELLULOSE," *Ind. Eng. Chem.*, vol. 54, no. 9, pp. 20–29, Sep. 1962, doi: 10.1021/ie50633a003.

[25] W. Ishak, I. Ahmad, S. Ramli, and M. C. I. Mohd Amin, "Gamma Irradiation-Assisted Synthesis of Cellulose Nanocrystal-Reinforced Gelatin Hydrogels," *Nanomaterials*, vol. 8, p. 749, 2018, doi: 10.3390/nano8100749.

[26] R. Gaudreault, T. Whitehead, and T. van de Ven, *Salt Necessary for PEO-Cofactor Association: The Role of Molecular Modelling in PEO Flocculation Mechanisms*. 2005.

[27] M. S. Reid, M. Villalobos, and E. D. Cranston, "Benchmarking Cellulose Nanocrystals: From the Laboratory to Industrial Production," *Langmuir*, vol. 33, no. 7, pp. 1583–1598, Feb. 2017, doi: 10.1021/acs.langmuir.6b03765.

[28] S. Beck-Candanedo, M. Roman, and D. G. Gray, "Effect of Reaction Conditions on the Properties and Behavior of Wood Cellulose Nanocrystal Suspensions," *Biomacromolecules*, vol. 6, no. 2, pp. 1048–1054, Mar. 2005, doi: 10.1021/bm049300p.

[29] W. Y. Hamad and T. Q. Hu, "Structure–process–yield interrelations in nanocrystalline cellulose extraction," *Can. J. Chem. Eng.*, vol. 88, no. 3, pp. 392–402, Jun. 2010, doi: https://doi.org/10.1002/cjce.20298.

[30] L. Chen, Q. Wang, K. Hirth, C. Baez, U. P. Agarwal, and J. Y. Zhu, "Tailoring the yield and characteristics of wood cellulose nanocrystals (CNC) using concentrated acid hydrolysis," *Cellulose*, vol. 22, no. 3, pp. 1753–1762, 2015, doi: 10.1007/s10570-015-0615-1.

[31] K. J. De France, K. G. Yager, T. Hoare, and E. D. Cranston, "Cooperative Ordering and Kinetics of Cellulose Nanocrystal Alignment in a Magnetic Field," *Langmuir*, vol. 32, no. 30, pp. 7564–7571, Aug. 2016, doi: 10.1021/acs.langmuir.6b01827.

[32] D. Bordel, J.-L. Putaux, and L. Heux, "Orientation of native cellulose in an electric field.," *Langmuir*, vol. 22, no. 11, pp. 4899–4901, May 2006, doi: 10.1021/la0600402.
[33] J.-F. Revol, H. Bradford, J. Giasson, R. H. Marchessault, and D. G. Gray, "Helicoidal self-ordering of cellulose microfibrils in aqueous suspension," *Int. J. Biol. Macromol.*, vol. 14, no. 3, pp. 170–172, 1992, doi: https://doi.org/10.1016/S0141-8130(05)80008-X.
[34] G. Nyström, M. Arcari, J. Adamcik, I. Usov, and R. Mezzenga, "Nanocellulose Fragmentation Mechanisms and Inversion of Chirality from the Single Particle to the Cholesteric Phase," *ACS Nano*, vol. 12, no. 6, pp. 5141–5148, Jun. 2018, doi: 10.1021/acsnano.8b00512.
[35] P.-X. Wang, W. Y. Hamad, and M. J. MacLachlan, "Structure and transformation of tactoids in cellulose nanocrystal suspensions," *Nat. Commun.*, vol. 7, no. 1, p. 11515, 2016, doi: 10.1038/ncomms11515.
[36] R. D. Deegan, O. Bakajin, T. F. Dupont, G. Huber, S. R. Nagel, and T. A. Witten, "Capillary flow as the cause of ring stains from dried liquid drops," *Nature*, vol. 389, no. 6653, pp. 827–829, 1997, doi: 10.1038/39827.
[37] X. Mu and D. G. Gray, "Droplets of cellulose nanocrystal suspensions on drying give iridescent 3-D 'coffee-stain' rings," *Cellulose*, vol. 22, no. 2, pp. 1103–1107, 2015, doi: 10.1007/s10570-015-0569-3.
[38] C. Zhang, X. Wang, and L. Qiu, "Circularly Polarized Photodetectors Based on Chiral Materials: A Review ," *Frontiers in Chemistry* , vol. 9. 2021, [Online]. Available: https://www.frontiersin.org/articles/10.3389/fchem.2021.711488.
[39] S. Beck, J. Bouchard, and R. Berry, "Controlling the Reflection Wavelength of Iridescent Solid Films of Nanocrystalline Cellulose," *Biomacromolecules*, vol. 12, no. 1, pp. 167–172, Jan. 2011, doi: 10.1021/bm1010905.
[40] X. Mu and D. G. Gray, "Formation of Chiral Nematic Films from Cellulose Nanocrystal Suspensions Is a Two-Stage Process," *Langmuir*, vol. 30, no. 31, pp. 9256–9260, Aug. 2014, doi: 10.1021/la501741r.
[41] A. Tran, C. E. Boott, and M. J. MacLachlan, "Understanding the Self-Assembly of Cellulose Nanocrystals—Toward Chiral Photonic Materials," *Adv. Mater.*, vol. 32, no. 41, p. 1905876, Oct. 2020, doi: https://doi.org/10.1002/adma.201905876.
[42] D. Nunes *et al.*, "Metal oxide nanostructures for sensor applications," *Semicond. Sci. Technol.*, vol. 34, no. 4, p. 43001, 2019, doi: 10.1088/1361-6641/ab011e.
[43] Ü. Özgür and H. Morkoç, "Chapter 5 - Optical Properties of ZnO and Related Alloys," C. Jagadish and S. B. T.-Z. O. B. Pearton Thin Films and Nanostructures, Eds. Oxford: Elsevier Science Ltd, 2006, pp. 175–239.
[44] M. Dong, Y. Wang, Z. Li, Z. Weng, and N. Yu, "Simple fabrication of homogeneous ZnO core/shell nanorod arrays for ultraviolet photodetectors," *J. Nanosci. Nanotechnol.*, vol. 18, no. 8, pp. 5686–5691, 2018.
[45] H. Makhlouf *et al.*, "Analysis of ultraviolet photo-response of ZnO nanostructures prepared by electrodeposition and atomic layer deposition," *Appl. Surf. Sci.*, vol. 444, pp. 253–259, 2018, doi: https://doi.org/10.1016/j.apsusc.2018.02.289.
[46] T. Park, K. E. Lee, N. Kim, Y. Oh, J.-K. Yoo, and M.-K. Um, "Aspect ratio-controlled ZnO nanorods for highly sensitive wireless ultraviolet sensor applications," *J. Mater. Chem. C*, vol. 5, no. 46, pp. 12256–12263, 2017, doi: 10.1039/C7TC04671E.
[47] W. Tian *et al.*, "Flexible Ultraviolet Photodetectors with Broad Photoresponse Based on Branched ZnS-ZnO Heterostructure Nanofilms," *Adv. Mater.*, vol. 26, no. 19, pp. 3088–3093, May 2014, doi: https://doi.org/10.1002/adma.201305457.
[48] N. Nasiri, R. Bo, F. Wang, L. Fu, and A. Tricoli, "Ultraporous Electron-Depleted ZnO Nanoparticle Networks for Highly Sensitive Portable Visible-Blind UV

Photodetectors," *Adv. Mater.*, vol. 27, no. 29, pp. 4336–4343, Aug. 2015, doi: https://doi.org/10.1002/adma.201501517.

[49] L. Duan *et al.*, "Fabrication of Self-Powered Fast-Response Ultraviolet Photodetectors Based on Graphene/ZnO:Al Nanorod-Array-Film Structure with Stable Schottky Barrier," *ACS Appl. Mater. Interfaces*, vol. 9, no. 9, pp. 8161–8168, Mar. 2017, doi: 10.1021/acsami.6b14305.

[50] J. Gong, J. Li, J. Xu, Z. Xiang, and L. Mo, "Research on cellulose nanocrystals produced from cellulose sources with various polymorphs," *RSC Adv.*, vol. 7, pp. 33486–33493, Jun. 2017, doi: 10.1039/C7RA06222B.

[51] L. Segal, J. J. Creely, A. E. Martin, and C. M. Conrad, "An Empirical Method for Estimating the Degree of Crystallinity of Native Cellulose Using the X-Ray Diffractometer," *Text. Res. J.*, vol. 29, no. 10, pp. 786–794, Oct. 1959, doi: 10.1177/004051755902901003.

[52] W. Hamad, *Cellulose nanocrystals: Properties, production and applications*. 2017.

[53] P. Lu and Y.-L. Hsieh, "Preparation and properties of cellulose nanocrystals: Rods, spheres, and network," *Carbohydr. Polym.*, vol. 82, no. 2, pp. 329–336, 2010, doi: https://doi.org/10.1016/j.carbpol.2010.04.073.

[54] V. Landry, A. Alemdar, and P. Blanchet, "Nanocrystalline Cellulose: Morphological, Physical, and Mechanical Properties," *For. Prod. J.*, vol. 61, no. 2, pp. 104–112, Mar. 2011, doi: 10.13073/0015-7473-61.2.104.

[55] K. Zhang, E. Brendler, and S. Fischer, "FT Raman investigation of sodium cellulose sulfate," *Cellulose*, vol. 17, no. 2, pp. 427–435, 2010, doi: 10.1007/s10570-009-9375-0.

[56] N. H. Turner, J. S. Murday, and D. E. Ramaker, "Quantitative determination of surface composition of sulfur bearing anion mixtures by Auger electron spectroscopy," *Anal. Chem.*, vol. 52, no. 1, pp. 84–92, Oct. 1980, doi: 10.1021/ac50051a021.

A ANNEXES

A.1 Electrical Characterization

Figure A1 presents the complete characterization of the flexible sensor.

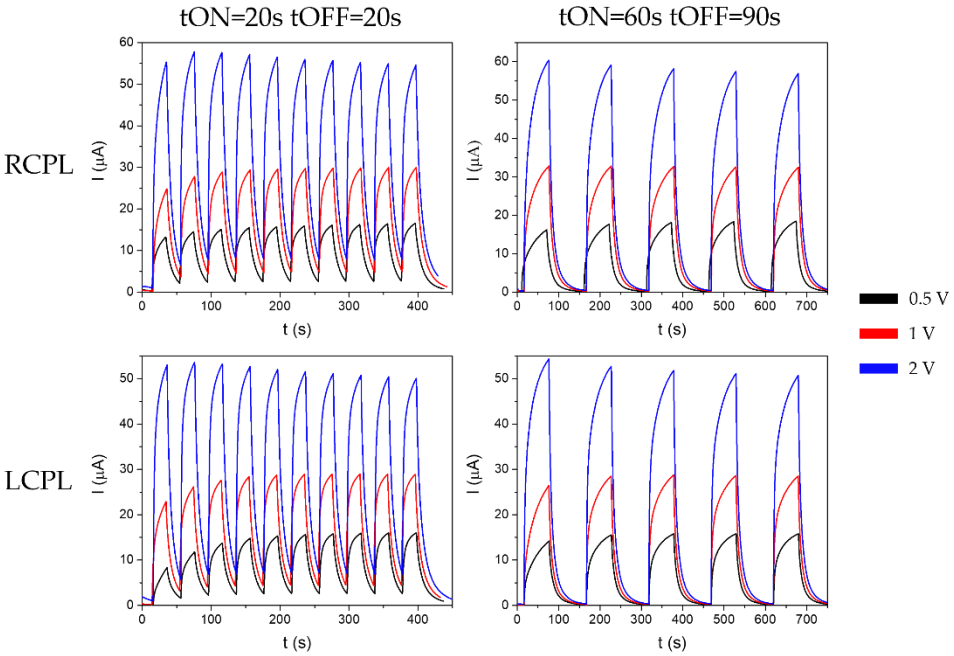

Figure A 1 - Electrical characterization of the flexible sensor, for both CPL polarizations and time intervals.